Permeability heterogeneity of sandstone intrusion fluid-escape systems, Panoche Hills, California: Implications for sedimentary basins globally.

Ben Callow[1,2*], Ismael Himar Falcon-Suarez[3], Jonathan M. Bull[1], Thomas M. Gernon[1], Sean Ruffell[1,4], Antonio Grippa[5,6] & Andrew Hurst[5].

[1]University of Southampton, School of Ocean and Earth Science, National Oceanography Centre Southampton, Southampton, SO14 3ZH, UK.

[2]Ghent University, Department of Geology, PProGRess/UGCT, Ghent, Belgium.

[3]National Oceanography Centre, Waterfront Campus, Southampton, SO14 3ZH, UK.

[4]Durham University, Department of Earth Sciences, Durham, DH1 3LE, UK.

[5]University of Aberdeen, School of Geosciences, Aberdeen, AB24 3FX, UK.

[6]Aker BP ASA, Jåttåvågveien 10, Hinna Park, 4020 Stavanger, Norway.

*Corresponding author (e-mail: ben.callow@ugent.be)

Keywords: Permeability, Cementation, Fluid flow, Sandstone intrusion, X-ray micro-CT, Seal bypass.

Abstract

Natural surface gas seeps provide a significant input of greenhouse gas emissions into the Earth's atmosphere and hydrosphere. The gas flux is controlled by the properties of underlying fluid-escape conduits, which are present within sedimentary basins globally. These conduits permit pressure-driven fluid flow, hydraulically connecting deeper strata with the Earth's surface; however they can only be fully resolved at sub-seismic scale. Here, a novel minus-cement-and-matrix permeability method using 3D X-ray micro-CT imaging enables the improved petrophysical linkage of outcrop and sub-surface data. The methodology is applied to the largest known outcrop of an inactive fluid-escape system, the Panoche Giant Intrusion Complex in Central California, where samples were collected along transects of the 600-800 m stratigraphic depth range to constrain porosity and permeability spatial heterogeneity. The presence of silica cement and clay matrix within the intergranular pores of sand intrusions are the primary control of porosity (17-27 %) and permeability (≤ 1 to ~500 mD) spatial heterogeneity within the outcrop analogue system. Following the digital removal of clay matrix and silica (opal-CT and quartz) cement derived from the mudstone host strata, the sand intrusions have porosity-permeability ranges of ~30-40 % and 10^3-10^4 mD. These calculations are closely comparable to active sub-surface systems in sedimentary basins. Field observations revealed at decreasing depth, the connected sand intrusion network reduces in thickness and becomes carbonate cemented, terminating at carbonate mounds formed from methane escape at the seafloor. A new conceptual model integrates the pore-scale calculations and field-scale observations to highlight the key processes that control sand intrusion permeability, spatially and temporally. The study demonstrates the control of matrix and cement addition on the physical properties of fluid-escape conduits, which has significance for hydrocarbon reservoir characterisation and modelling, as well as subsurface CO_2 and energy storage containment assessment.

1 Introduction

Onshore and offshore surface gas seeps originating from subsurface geological sources provide a substantial flux of greenhouse gas emissions into the Earth's atmosphere and hydrosphere, which affects global climate. Annual global methane emissions supplied from natural geological sources are quantified as 18-63 Mt, with offshore seeps contributing 5-10 Mt, with significant uncertainty in the calculations (Etiope et al., 2019; Foschi et al., 2020; Saunois et al., 2020). Understanding gas flux rates from onshore and offshore seeps is needed to more precisely quantify the natural input of greenhouse gases into the atmosphere and hydrosphere (Leifer and Boles, 2005; Shakhova et al., 2010; Greinert et al., 2010). The flux rates are controlled by underlying fluid-escape conduits, sealbypass systems which include connected fault and fracture networks, sandstone intrusions and seep structures, present within sedimentary basins globally (Cartwright et al., 2007; Løseth et al., 2009; Andresen, 2012; Karstens and Berndt, 2015). These seal bypass systems permit cross-stratal pressure-driven focused fluid flow, hydraulically connecting deeper strata with the Earth's surface (Cartwright et al., 2007). In addition, these systems may provide leakage pathways through the overburden, where directly overlying prospective reservoirs for subsurface carbon dioxide, energy or waste storage (Karstens et al., 2017). A detailed understanding of the geometry, permeability and composition of seal bypass structures is crucial to improving risk assessments and quantifying subsurface fluid-escape fluxes.

Sand injection complexes are regionally-developed seal bypass features (10's to 1,000's km^2) that form in the shallow crust in response to short-lived (hours to weeks) periods of supra-lithostatic pore-fluid pressure (Vigorito and Hurst, 2010). They form by the forceful injection of fluidised sand, largely in turbulent flow, into actively propagating hydraulic fractures (Hurst et al., 2011). Once emplaced they form highly connected sandstone intrusion

networks, in otherwise low permeability host strata that may enable vertical fluid transference from within the host and deeper strata, toward Earth's surface (Hurst et al., 2003a; Cartwright et al., 2007; Grippa et al., 2019). Sand intrusions may enhance fluid transmissivity perpendicular to bedding, creating high permeability pathways through intrinsically low permeability fine-grained strata (Grippa et al., 2019). Discordance with bedding is a key diagnostic of all sandstone intrusions and at all scales of observation (Hurst et al., 2011). Individual sandstone intrusions are most commonly composite (Huuse et al., 2007; Scott et al., 2009; Satur et al., 2021), and vary in size from km-scale length and 10's m thickness to cm-scale length and thickness (Fig. 1). Independently of the size and geometry of individual intrusions, they commonly exhibit fine to medium grain size distributions, which is attributed primarily to preferential entrainment of smaller grains into particle suspension, as well as preferential abrasion of larger grains during sand fluidization (Hurst et al., 2003b; Gera et al., 2004; Hurst et al., 2011; Hurst et al., 2021a). Sandstone intrusions are a form of seal bypass feature, however they are also widely recognised as prospective hydrocarbon reservoirs (Briedis et al., 2007; Huuse et al., 2007).

Using seismic reflection imaging, sand intrusions become more difficult to detect with increasing discordance to host strata bedding (Huuse et al., 2007; Grippa, et al., 2019). 3D seismic surveys resolve the characteristic discordance of low-angle to bedding intrusions, while thin (<5-10 m) and steep (>40° to bedding) intrusions are rarely resolved and commonly undetected by seismic as they are beyond seismic resolution (Huuse et al., 2007; Grippa et al., 2019). Also, constructive and destructive tuning effects caused by varying angles of bedding discordance alter sandstone intrusion apparent thickness and geometry inferred from 3D seismic (Grippa et al., 2019). In addition, borehole data may fail to differentiate between parent depositional units and sandstone intrusions, when they have

similar mineralogy (Briedis et al., 2007; Lonergan et al., 2007). Dipmeter or borehole image data can identify discordance between bedding and intrusions with confidence, particularly if some drillcore is available for calibration (Duranti et al., 2002; Satur et al., 2021). Detailed study of onshore outcrop analogues has enabled sub-seismic scale characterisation of sand intrusions (e.g., Ross et al., 2014; Cobain et al., 2015).

Petrographic and mineralogical characterisation of subsurface sandstone intrusions has received relatively little attention (Duranti et al., 2002) in comparison to outcrop studies (Scott et al., 2009; Bouroullec and Pyles, 2010; Ravier et al. 2015; Zvirtes et al., 2020). Petrographic studies of sandstone intrusions (Duranti and Hurst, 2004; Scott et al., 2009; Hurst et al., 2021a) revealed their (2D) textural immaturity and high content of detrital matrix, relative to depositional parent sandstone. Advances in 3D X-ray micro-computed tomography (µCT) image acquisition systems (Bodey and Rau, 2017), combined with µCT image-processing methods more suitable for analysing compositionally heterogeneous samples (Callow et al., 2020) provide an opportunity to quantify the physical and textural properties of heterogeneous sediment samples non-invasively, and with improved accuracy compared to previous preliminary insights (Wu et al., 2017). The µCT method allows in situ sample properties to be preserved. In comparison to conventional laboratory methods, µCT does not require invasive sample preparations (e.g., thin sections), or the need to modify the original stress state of the sample (e.g., flow-through testing) which can induce significant changes to grain fabric of poorly consolidated samples, that directly affects physical property calculations (e.g., Falcon-Suarez et al., 2020).

In this paper, sand intrusion outcrops in the San Joaquin basin, Panoche Hills, Central California have been characterised. The Panoche Giant Intrusion Complex (PGIC) is the

largest known outcrop exposure of sand intrusions on Earth, manifested on a spatial scale of > 400 km^2 outcrop exposure and ~1.5 km stratigraphic depth (Fig. 1; Vigorito and Hurst, 2010). Here, a novel three-dimensional μCT image processing and analysis technique is developed to digitally remove pore-filling cement and clay matrix from the intergranular pore volume (IGV) of sandstone intrusion samples. This approach permits the 3D pore-scale investigation of the effect of cement and clay matrix inside the intergranular pore volume (IGV) on the porosity and permeability of sandstone intrusions, that previously was limited to 2D analysis (Scott et al., 2013; Ravier et al., 2015). This paper has two main research hypotheses, which form the primary research aims:

1) Hurst et al. (2021a) revealed the (2D) textural immaturity and high content of detrital matrix in sandstone intrusions of the PGIC, relative to depositional parent sandstones. Therefore, it is first hypothesised that the pore-filling detrital clay matrix and cement are the primary control for porosity and permeability at the pore-scale, and therefore accounts for porosity-permeability spatial heterogeneity at the field-scale within the Panoche Giant sandstone Intrusion Complex (PGIC). The hypothesis will be tested using the minus-cement-and-matrix μCT image methodology. Further, detailed petrological analysis of the cement and matrix material, combined with field-scale observations, will also permit a developed understanding of how the cement and matrix formed, and when it was emplaced.

2) Secondly, it is hypothesised that the processes contributing to the presence of cement and clay matrix, which include mudstone matrix addition and cement growth, are a more site-specific feature of the Panoche Hills Giant Intrusion Complex (PGIC) outcrop when compared to subsurface analogues. Therefore, the micro-textural observations and physical properties of the outcrop analogue will be compared with previous studies of subsurface sandstone intrusions in the North Sea, such as the Volund Field (Satur et al., 2021) and the Alba Field (Duranti and Hurst, 2004). Given that the PGIC is the most well-recognised

outcrop analogue for sandstone intrusions globally (Hurst et al., 2011), which sub-seismic scale sandstone intrusion reservoir models are designed upon, this has major significance. The pore-scale findings, combined with the field-scale observations, enable the creation of a schematic, conceptual model for the overall geometry, composition and permeability of sandstone intrusion fluid-escape systems, and an assessment of how these properties vary temporally and spatially, which can be used to produce realistic process-based fluid simulation and reactive transport models for hydrocarbon reservoir modelling, or for assessments of fluid leakage through the overburden (Marin-Moreno et al., 2019).

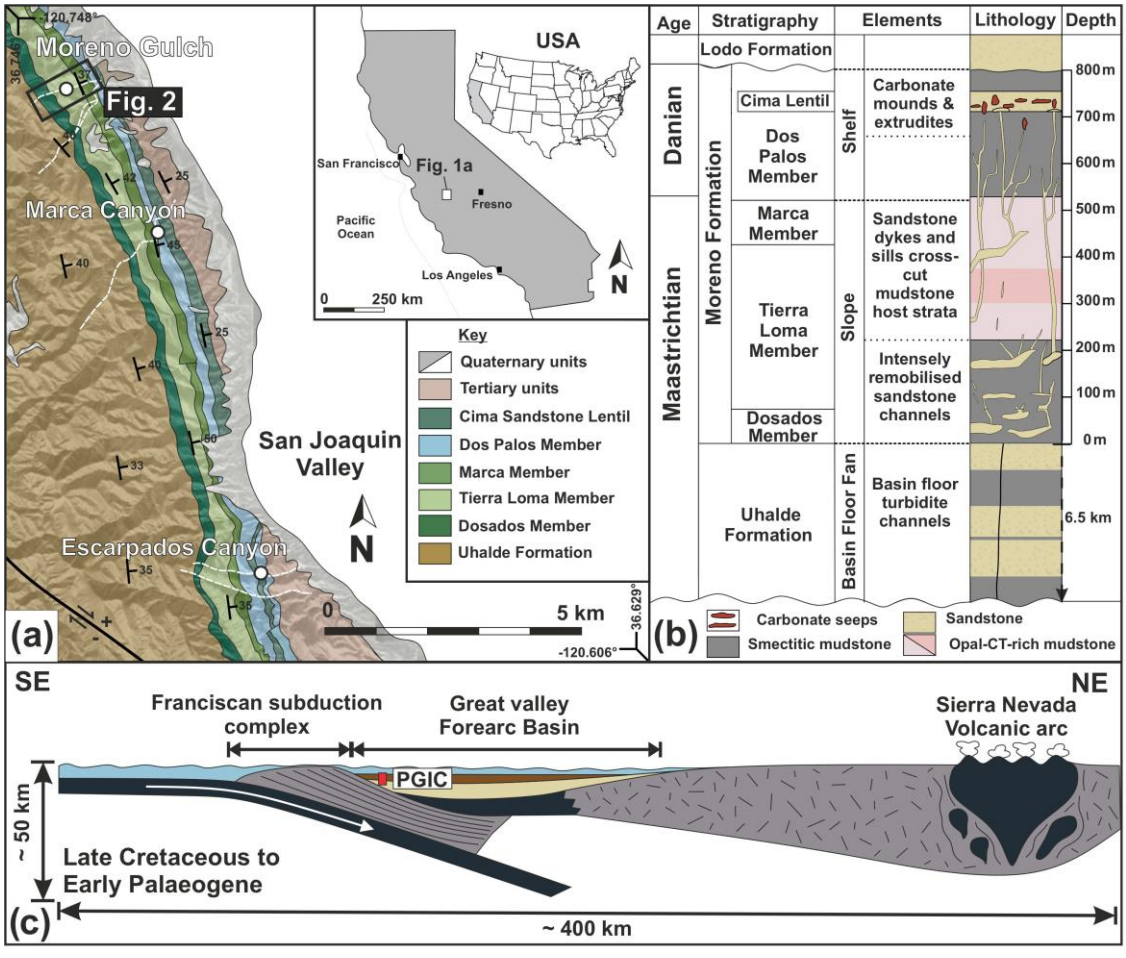

Figure. 1. Regional geological map and stratigraphy of the Panoche Hills field site, central California. **a)** A Geological map of the Panoche Hills is overlaid onto a Google Earth satellite map. There is a regional 35° north-easterly dip of the rock units towards the San Joaquin Valley. Black box indicates area displayed in Fig. 2. **b)** A lithostratigraphic column, for the Panoche Giant Injection Complex

(PGIC), a sequence of sand intrusions is present within the Moreno Formation. **c)** A simplified diagram (after Ingersoll, 1979) of the Great Valley forearc basin regional tectonics during the Late Cretaceous to Palaeogene. The PGIC is located on the western margin of the Great Valley forearc basin.

2 Geological Setting

The Panoche Hills field outcrop is a type example of a naturally occurring fluid-escape system. The field site is located on the western margin of the San Joaquin Basin in Central California (Fig. 1). The Panoche Hills comprise Mesozoic strata of the Great Valley Group, originally deposited in a forearc basinal setting (Fig. 1) (Ingersoll, 1979). This basin was part of a compressive system related to subduction of the Pacific plate, which commenced during the Late Jurassic (Fig. 1) (Ingersoll, 2019). Uplift of the Great Valley Basin's western margin commenced in the Quaternary and continues to the present day. The field site has close to 100 % exposure and steeply dipping beds (Figs. 1-2), allowing the fluid-escape system structure, geometry and spatial variability to be constrained.

Marine sediments of the Great Valley Group were deposited from the Late Cretaceous (Cenomanian stage) to the Early Palaeocene (Danian stage), and are unconformably overlain by Late Palaeocene to Middle Eocene sediment (Ingersoll, 1979). The Upper Cretaceous to Early Palaeocene (Danian stage) succession of the Panoche Hills comprises two main formations (Fig. 1). Firstly, the top of the Panoche Fm. (also termed Uhalde Fm.) is composed of interbedded sandstone sub-marine fan deposits, separated by mudstone intervals (Bartow, 1996). The Moreno Fm. conformably overlies the Panoche Fm., representing a transition from a deep marine to shelf setting (Fig. 1b). The Moreno Fm. comprises four main members: (1) Dosados Member, (2) Tierra Loma Member, (3) Marca Member and (4) Dos Palos Member, which contains the sub-unit Cima Lentil (Fig. 1b) (Bartow, 1996; Vigorito et al., 2008).

Emplacement of the PGIC in the early Palaeocene was caused by pore-fluid overpressure in the sandstone-rich lower part of the Moreno Formation exceeding the lithostatic gradient (Vigorito and Hurst, 2010). A period of regional tectonic compression preceded PGIC initiation, but, to date, causal relationships between the regional compression and sand injection have not been established. Intense hydraulic fracturing of overlying mudstone host strata occurred as an immediate precursor to sand injection. Sandstone intrusions in the PGIC have both steep discordance (dykes) and shallow discordance (sills) to bedding; dykes have a near perpendicular orientation to bedding (Vigorito and Hurst, 2010). Sandstone in the PGIC is a hydraulically-connected system, comprising a lower dyke zone, sill zone and upper dyke zone (Fig. 2) (Vigorito et al., 2008; Vigorito and Hurst, 2010). Injected sand acted as a fracture proppant, creating permanent fluid-escape pathways that extended through 100s m of overburden, and, in some cases, they reached the palaeo-seafloor (Minisini and Schwartz, 2007; Vigorito et al., 2008).

Sand extrudites and methane-derived authigenic carbonates (MDACs) within the Cima Lentil Member are the shallowest stratigraphic level associated with the PGIC (Vigorito et al., 2008; Vigorito and Hurst, 2010). MDACs are present at active seabed methane ebullition sites (Judd and Hovland, 2009). Dating of the carbonates (MDACs) therefore constrains the timing of sand injection to 66 Ma (66-62 Ma) (Danian; Minisini and Schwartz, 2007; Blouet et al., 2017) and indicates that seabed gas seeps remained active for ~2 Ma (Minisini and Schwartz, 2007).

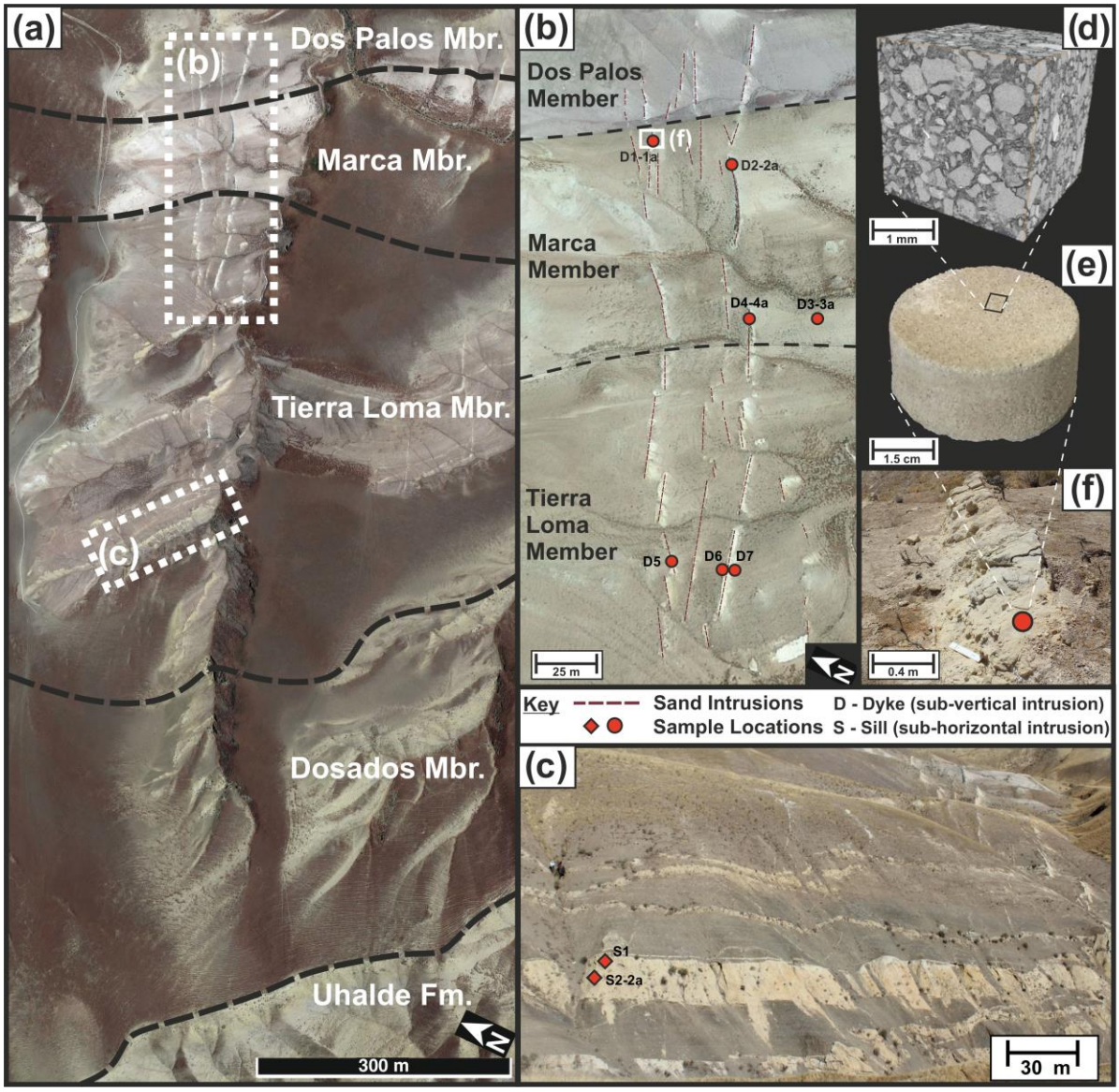

Figure. 2. Sand intrusion sampling locations, collected in Moreno Gulch, Panoche Hills. **a)** The Google Earth satellite map displays the two primary sampling locations within Moreno Gulch: **b)** The upper dyke zone and **c)** The sill zone. Red circles - sub-vertical sand intrusions - D; Red diamonds - sub-horizontal intrusions - S. **b)** The sand intrusion network - dark red dashed lines, is oriented perpendicular to bedding strike direction - black dashed lines. **d-f)** 5cm diameter core plugs were sampled (e) and analysed using 3D X-ray micro-CT imaging (d). Two samples were collected at five locations (e.g., 1-1a; Supplementary Fig. S1 provides additional images of each sampling location).

3 Materials and methods

3.1 Rock samples

Fieldwork was conducted in Moreno Gulch, Marca Canyon and Escarpados Canyon (Fig. 3), across a 600-800 m vertical stratigraphic succession of the Moreno Fm. (Fig. 2; Supplementary Fig. S1). Moreno Gulch was selected as the primary field sample location, as the outcrop exposure permitted sampling across the full 600 - 800 m stratigraphic range. Sand intrusion samples were collected from Moreno Gulch, along ridgeline transects parallel to bedding (along strike), at multiple stratigraphic depth intervals (Fig. 2). Along those transects, samples were taken at random locations, in order to minimise self-selection sampling bias. A total of 15 samples were collected from three selected intervals of the dyke zone (D1-D7), and one interval of the sill zone (S1-S2). In five locations, two samples were collected (e.g., D1 and D1a), to account for localised (cm to m-scale) heterogeneity. Oriented samples were collected from buried, unweathered surfaces, which were dug out and extracted from below the surface regolith, to minimise the affects of surface weathering processes. Field observations and structural measurements were also recorded, including sandstone intrusion orientation, thickness and spacing (Supplementary Table S1). In addition, an independent study collected three mudstone host strata samples, from Right Angle Canyon, that are representative of each main host rock member (Tierra Loma, Marca and Dos Palos) (Hurst et al., 2021b).

From each sample collected in the field, ~25 mm length, 50 mm diameter core plugs are extracted for porosity and permeability determinations in the laboratory (Callow et al., 2020), and 10 mm diameter plugs for 3D X-ray micro-CT (μCT) image analysis (Fig. 2; Supplementary Fig. S1-S2). Additionally, thin sections (30 μm thickness) were prepared for transmitted light microscopy and Scanning Electron Microscopy (SEM), permitting a detailed

assessment of sample texture and composition. SEM imaging was performed with a Carl Zeiss Leo 1450 VP scanning electron microscope (SEM) with an energy dispersive spectrometer (EDX) (Carl Zeiss AG, Jena, Germany). The sandstone intrusion and host strata mudstone samples were carbon coated and imaged at a pixel resolution of less than 1.5 µm. The elemental composition of each phase was verified using SEM-EDX analysis. Independent XRD (X-ray diffraction) and XRF (X-ray fluorescence) analyses verified the mineralogy and bulk chemistry of the samples, which is further described in Hurst et al. (2021b).

3.2 X-ray micro-CT Image Analysis

µCT image acquisition was conducted using an X-ray synchrotron source (Diamond Light Source, Beamline I13-2, Oxford, UK), using a pink beam in the energy range of 20-30 keV. Scans were performed on cylindrical samples of 10 mm diameter by 25 mm height, and were scanned in dry state (oven-dried at 40°C). The samples were held onto the rotation stage with SEM stubs, which are glued to the sample base. Scans were acquired using a 4 x optic and PCO Edge 5.5 scintillator-coupled detector in full frame mode (2560 x 2160 pixels) with a 0.032 magnification, resulting in a pixel resolution of 0.81 µm (Callow et al., 2020). 4000 equiangular projections were obtained through 360° with a 0.5 s exposure time per projection (25 minutes per scan) (Callow et al., 2020). Image phase contrast is determined by the relative X-ray attenuation of each solid grain and pore-filling phase (Ketcham and Carlson, 2001). A paganin filter (Delta/Beta = 150) was applied to the data during image reconstruction to further enhance the image phase-contrast (Callow et al., 2020). The 32-bit greyscale image volumes produced by the image reconstruction were converted into 8-bit and denoised using a non-local means filter. The high phase contrast images permitted the accurate segmentation and determination of each mineral grain and cement phase (air, quartz,

clay matrix and silica cement (opal-CT and quartz), carbonate and iron-oxide) (Supplementary Fig. S3). Image segmentation was performed using a 3D supervised machine learning technique (Weka) using open-source software (Supplementary Fig. S3) (Arganda-Carreras et al. 2017; Callow et al., 2020). The data were segmented into three classified phases: (1) air; (2) grains and (3) a combined clay matrix & silica (opal-CT) cement phase (Supplementary Fig. S3). The air phase (1) corresponds to the intergranular pores resolvable from the µCT image volume, and the grain phase (2) corresponds to the quartz and feldspar grains. The pore-filling clay matrix and silica (opal-CT) cement are estimated to contain 60-70 % intragranular microporosity, which lies below the µCT image resolution, which is calculated based on mass balance considerations (Callow et al. 2020) and literature microporosity estimates for smectite clay and silica (opal-CT) cement (Hurst & Nadeau 1995; Alansari et al. 2019).

µCT image-based analyses were used to quantify the physical properties of each sample, following a workflow outlined in Callow et al. (2020) (Supplementary Fig. S2). The calculations acquired included; (1) total and connected (effective) porosity; (2) pore and grain size distribution, and; (3) horizontal and vertical absolute permeability. (1) Connected (effective) porosity is defined as voxels assigned to the air phase which are connected by a common face. Total porosity is defined as voxels classified to the air phase combined with 65 % of the voxels classified to the combined clay matrix and cement phase, thereby accounting for the intergranular porosity and estimated intragranular microporosity (Supplementary figure S3). (2) Pore and grain size distributions are calculated by performing a distance transform and watershed transform to the classified air and grain phases of the µCT image volume, respectively (Callow et al. 2020). The transform functions enable the separation and labelling of each pore and grain, which permits the calculation of pore and grain diameter

size distribution (Supplementary figure S2). The minimum pore diameter is limited by the 0.81 µm voxel size of the 3D image volumes. (3) Horizontal and vertical absolute permeability simulations determinations are calculated using a Naiver-Stokes finite-element flow solver (Avizo, 2018). The intragranular microporosity of the combined clay and cement phase are assumed to be impermeable, therefore the simulation is applied to the voxels assigned to the connected pore (air) phase. Further details of the physical property calculations are described in Callow et al. (2020). Callow et al. (2020) performed an uncertainty analysis of image resolution, image segmentation, representative elementary volume and finite element volume simulation method for the samples used in this study, and determined that the porosity and absolute permeability calculations are accurate to ±1 % and within one order of magnitude, respectively. The pore size and absolute permeability were also calculated with the combined clay matrix and cement phase digitally removed. The process of digital removal of the clay matrix and silica (opal-CT) cement (CDR) reclassifies the combined clay matrix and cement phase to the air phase. Thus, the combined effect of cementation and clay matrix addition on the pore property calculations could be assessed.

4 Results

4.1 Field observations

4.1.1 Moreno Gulch

The sand intrusions within the Tierra Loma Mbr and Marca Mbr of the Moreno Fm. are discordant to bedding (dykes) (Fig. 3). The stereonet shows a rose diagram and poles-to-plane of dyke orientation, showing that the dykes are discordant to the ESE/WNW strike of the host rock strata (Fig. 3a). Distinct vertical layers are present within individual intrusions (Fig. 3c). At greater stratigraphic depths within the Tierra Loma Mbr, 200 m from the top of the stratigraphic unit, sandstone intrusions are concordant to bedding (sills) (Fig. 1). The

sandstone sills typically have convex upper margins which indicate previous episodes of the erosive, sub-horizontal flow of fluidised sediment.

4.1.2 Marca Canyon

The sand intrusions extend to the top of the Dos Palos Member of the Moreno Fm. At shallower depths within the Moreno Fm., the thickness of the sandstone dykes decreases from m-scale to cm-scale thickness, and are carbonate cemented (Fig. 3d-g; Supplementary Table S1). Despite the decreasing intrusion thickness at shallower stratigraphic depths, the sandstone intrusions extend to a palaeo-seafloor, terminating at carbonate mound structures (Fig. 3e-g).

4.1.3 Escarpados Canyon

Within the Cima Sandstone Lentil Member, the carbonate mound structures extend laterally along one main stratigraphic horizon (Fig. 3). The carbonate mounds display a modal orientation of ESE/WNW strike and 40° dip, which is concordant to the host strata bedding orientation (Supplementary Table S2). Successive layers are present within the carbonates (Fig. 3h). Ichnofabrics provide evidence that the carbonate structures likely formed at the seafloor (Fig. 3k).

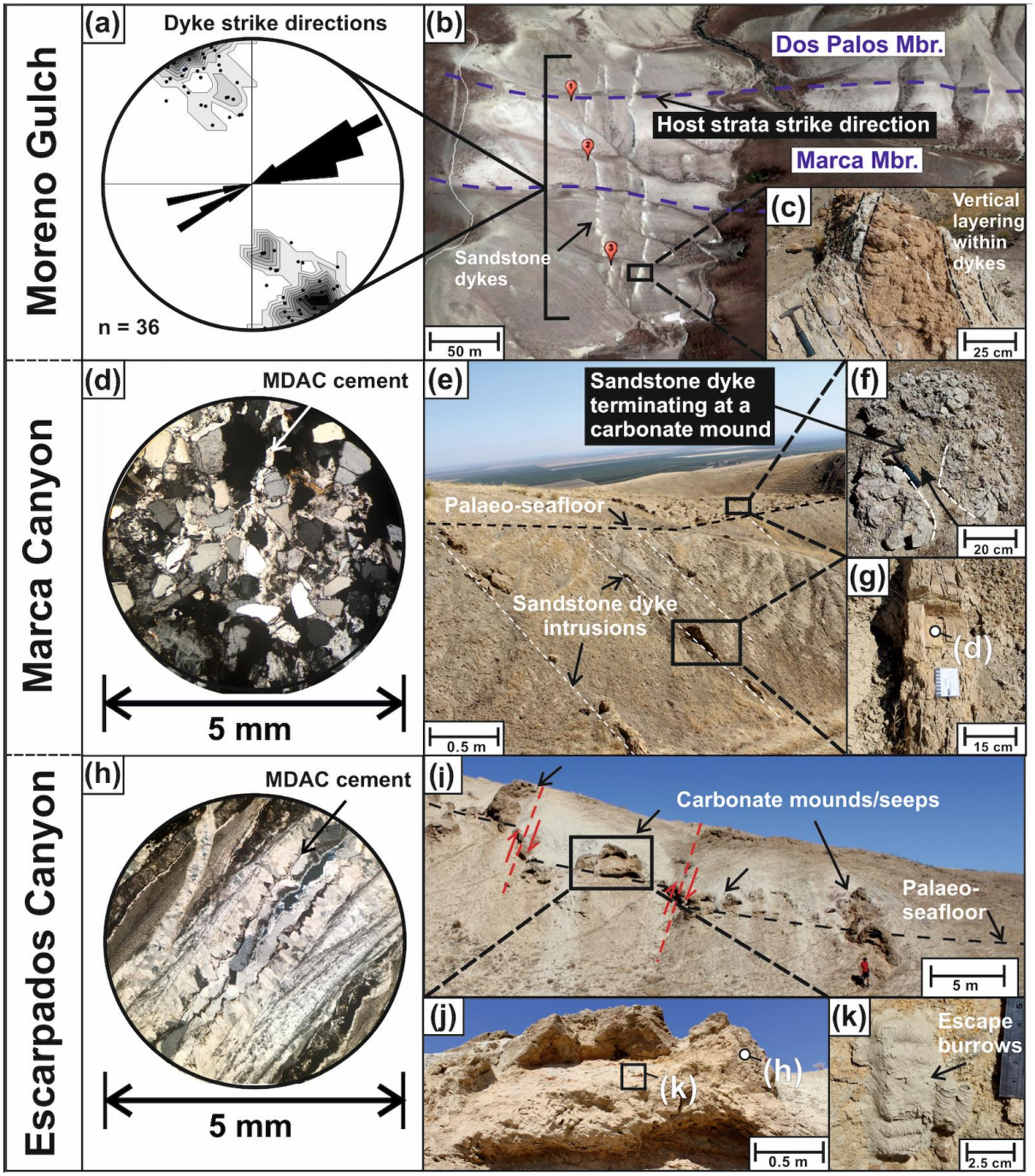

Figure. 3. Photographs highlighting key observations across the sand intrusion system from three main localities of the Panoche Hills field site: Moreno Gulch (a-c), Marca Canyon (d-g) and Escarpados Canyon (h-k). **Moreno Gulch: a)** Stereonet showing a modal ENE/WSW dyke orientation trend in Moreno Gulch, which is discordant to the ESE/WNW strike orientation of the host strata bedding (Supplementary Table S1). **b)** A view of the upper section of Moreno Gulch, with dykes oriented perpendicular to bedding. **c)** A cross-section through a sandstone dyke showing vertical layering, interpreted as multiple pulses of fluidised sediment flow. **Marca Canyon: d)** A thin section of a sandstone dyke, displaying carbonate cementation. **e)** Sandstone intrusions terminating at the carbonate mound horizon. **f)** Evidence for a sandstone intrusion terminating within a carbonate

mound. **g)** A carbonate cemented sandstone dyke. **Escarpados Canyon: h)** A thin section image from a carbonate mound sample, showing carbonate precipitation in discrete layers, which have accreted onto open fracture surfaces. **i)** A view of the carbonate mounds which have formed along one main horizon. **j)** A closer view of a carbonate mound, showing a sandy core, enveloped by an outer carbonate crust. **k)** An escape burrow (fugichnia) present within the sandy core of a carbonate mound.

4.2 Host rock properties

SEM analyses of the host rocks revealed that grain size increases from older to younger strata, transitioning from clay to silt-sized grains (Fig. 4). Sub-angular to angular quartz grains are matrix-supported (Fig. 4). SEM-EDS and XRD analyses revealed that the host rock samples are composed of silica (opal-CT and quartz) and smectite clay (Table 1). Smectite comprises ~90 % of the phyllosilicate components, with minor illite and kaolinite. Silica is enriched in the two deeper host rock members, comprising ~80 % of the non-phyllosilicate components (Table 1). Moulds of diatom test fragments are common, which explains the silica enrichment of the sample matrix (Fig. 4).

XRD analysis also shows the relative proportions of the silica mineral phases (Table 1). The opal-CT increases with depth, by up to 17% of the total sample volume. Conversely, opal A was not detected in any sample (Table 1). SEM imaging reveals 3-20 µm sized blade-like crystals that form sub-spherical features, present on relic diatom microfossil tests (Fig. 4).

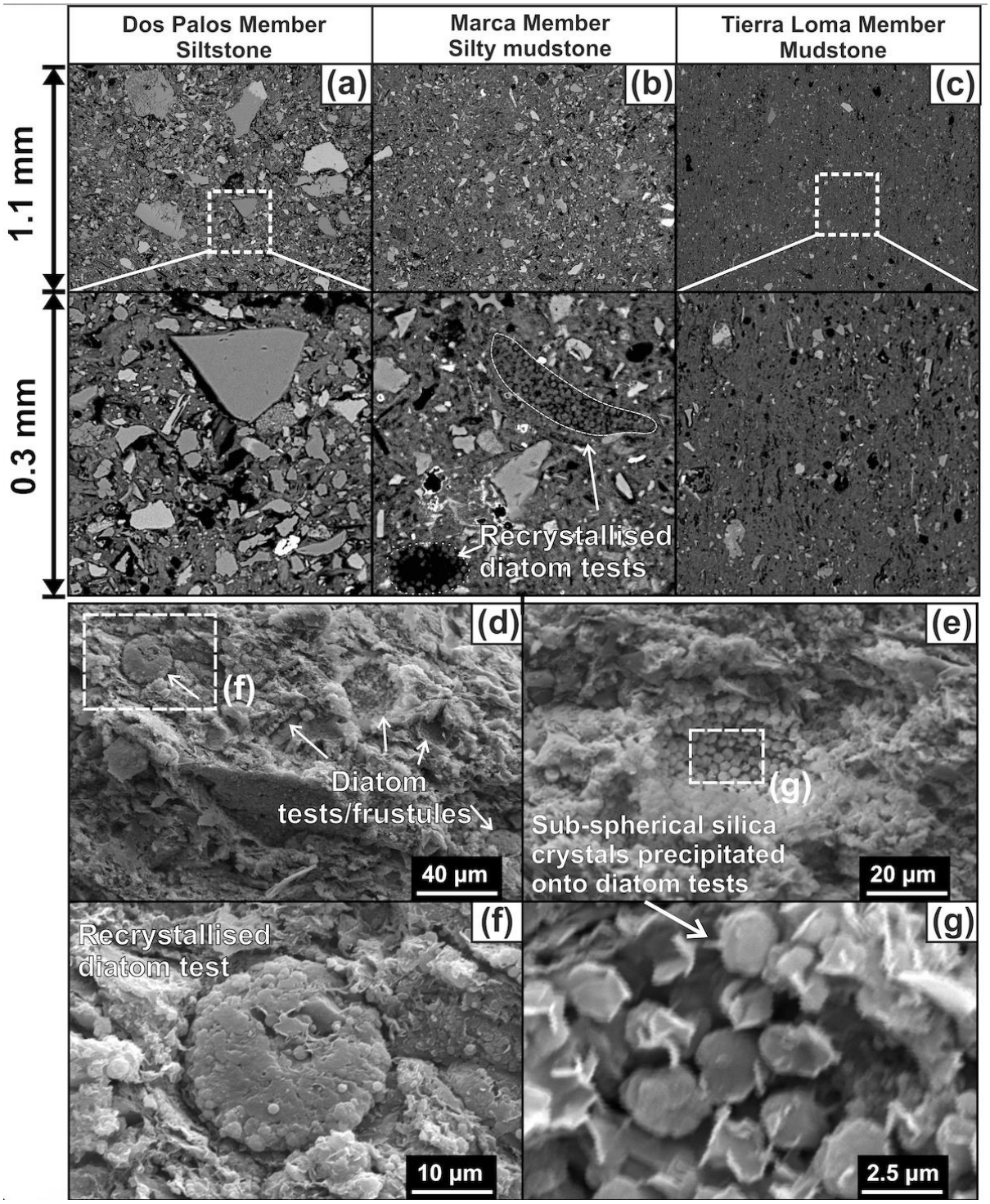

352

353 **Figure. 4.** Scanning Electron Microscopy images displaying the texture of the fine-grained host strata
354 of the Moreno Formation. **a)** Dos Palos Member - Siltstone; **b)** Marca Member - Silty mudstone; **c)**
355 Tierra Loma Member - Mudstone. SEM-EDX analysis reveals that all samples are siliceous (silica-
356 rich), composed of sub-angular quartz grains in a cement matrix of smectite clay and opal-CT. **d-g)**
357 Marca Member – evidence of fully recrystallised diatom tests (after Hurst et al. 2021b) highlights a
358 transition from opal-A to opal-CT.

359

Table 1. *XRD analysis of the host rock mudstones*

	Non-Phyllosilicates						Phyllosilicates			
Member	Qtz	Op CT	Op A	Crist	K-feld	Pl	Sm	Ill	Kao	∑Phy
Dos Palos	14.0	0.0	0.0	3.3	4.8	9.2	60.6	2.1	6.0	68.7
Marca	13.4	13.8	0.0	4.5	1.8	5.3	57.5	2.5	1.8	61.8
Tierra Loma	13.1	17.2	0.0	2.2	3.4	6.4	55.4	2.0	0.4	57.8

Qtz = quartz; Op Ct = Opal CT; Op A=Opal-A (amorphous silica); Crist = cristobalite; K-feld = K feldspars; Pl=plagioclase feldspar; Sm=smectite; Ill=Illite; Kao=kaolinite; ∑Phy=sum of phyllosilicates. After Hurst et al. (2021b).

Table 2. *Sand intrusion physical properties calculated from X-ray micro-CT image analysis*

Sample	**D1**	**D1a**	**D2**	**D2a**	**D3**	**D3a**	**D4**	**D4a**	**D5**	**D6**	**D7**	**S1**	**S2**	**S2a**
Φc (%)	12.9	15.3	1.2	3.5	7.5	6.1	8.9	7.8	8.8	8.3	14.8	13.4	17.1	18.6
Φt (%)	23.6	26.8	18.7	16.6	20.5	20.2	25.2	22.9	21.2	22.1	26.6	21.5	23.4	24.7
Clay/Cement (%)	20.5	22.1	29.8	22.9	23.9	25.5	31.3	28.6	23.1	25.0	22.8	15.7	12.1	11.9
D_D (μm)	69	70	n/a	n/a	67	68	69	68	69	69	69	73	69	70
Av. k (mD)	274	307	≤ 1	≤ 1	42	36	73	72	74	52	177	401	388	538
CDR Φt (%)	33.9	37.8	33.7	28.1	32.5	32.9	40.8	37.2	32.8	34.6	38.0	29.4	29.5	30.6
CDR Av. k (mD)	3209	4501	2098	1200	2439	2370	6274	4564	1872	2233	4535	3046	2505	2798

Φc = Connected porosity; Φt = total porosity, where it is assumed/estimated that the clay matrix and cement phases have a microporosity of 50%; Clay/Cement = clay matrix and cement fraction; D_D = Mean pore diameter; Av. k=Mean permeability, an average of vertical (kv) and horizontal (kh) permeability; CDR = Clay matrix and cement digitally removed. mD = millidarcies.

4.3 Sandstone intrusion properties

4.3.1 Grain size

Textural properties of sand intrusion have been evaluated using 3D µCT image data and transmitted light microscopy (Fig. 5). The samples are primarily composed of sub-angular to angular quartz grains. The mean grain sizes are comparable between the sill and dyke samples (~ 140 μm), with the former having a greater proportion of grains ≥300 μm diameter (Fig. 5). Hence, the sill samples are poorly sorted, relative to the moderately sorted dyke samples. Grain micro-fracturing is present in the dyke samples, in contrast to the sill samples (Fig. 5; Supplementary Fig. S7). All sample grain size distributions display a positive skewness (sk > 0.4), due to a high proportion of finer grains relative to the mean (Fig. 5). Petrographic analyses confirm that the pore-filling cement and clay matrix are mostly composed of silica (opal-CT and quartz) and smectite (Fig. 5), which is directly comparable to the mudstone host rock composition (Table 1; Fig. 4). The dyke samples displayed in Fig. 5a-b, represent two end-member samples of high (above 30%), and lower (below 30 %) silica (opal-CT) cement and clay matrix volume, respectively. The dyke samples have a higher proportion of pore-filling cement and clay matrix volume (20-30 %), relative to sill samples (12-16 %) (Table 2; Fig. 5). Overall, dyke samples display a lower textural maturity and a higher proportion of pore-filling silica (opal-CT) cement and smectite clay relative to sill samples.

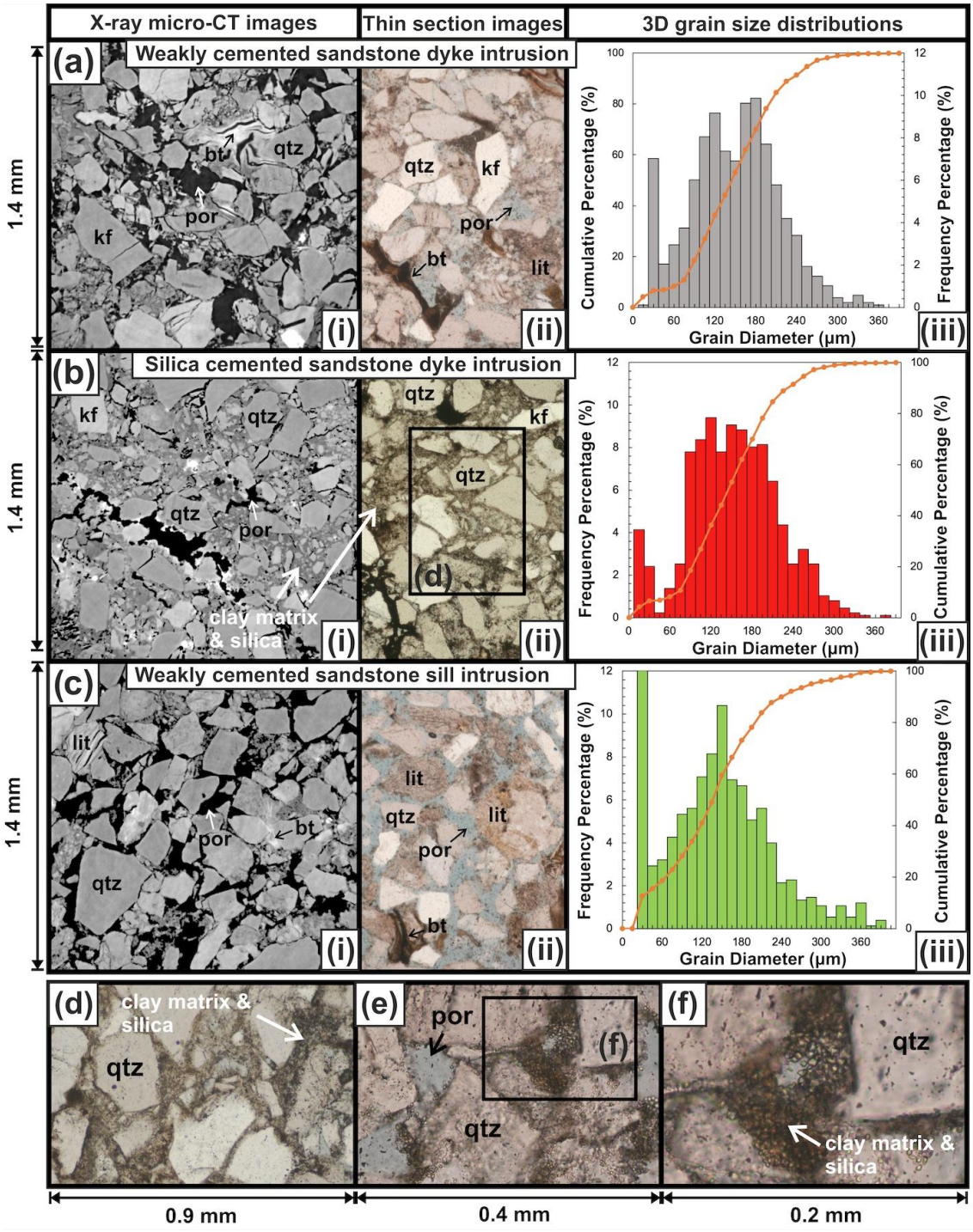

391

392 **Figure. 5.** 2D images displaying the textural and compositional variability of sandstone intrusions,
393 and their corresponding 3D grain size distributions. **a-c)** Displayed are a) weakly cemented and b)
394 cemented sub-vertical intrusions (dykes), as well as c) a sub-horizontal intrusion (sill). **i)** X-ray micro-
395 CT images. The greyscale reveals areas of low (black) to high (white) X-ray attenuation. **ii)** Thin
396 section images using plane polarised light microscopy. **iii)** Grain size distributions derived from 3D
397 X-ray micro-CT image analysis (see Callow et al., 2020 for further details of the methodology). **d-f)**
398 The clay matrix and cement are composed of a mixture of smectite clay and silica (opal-CT and
399 quartz). qtz – quartz; por – pore space; kf – k-feldspar; bt – biotite mica; lit – lithic grain.

400

401 *4.3.2 Porosity-Permeability*

402 Sandstone intrusions show connected and total porosity ranges between 1.2-18.6 % and 16.6-
403 26.8 %, respectively (Table 2). Sills have a higher connected porosity on average (16.4 %)
404 relative to the dykes (8.6 %), however their total porosities are comparable (23 and 22%;
405 Table 2). For dykes, non-connected (intragranular) pores represent ~60 % of the total pore
406 volume, while only 30 % on average for sills. This indicates that a significant proportion of
407 dyke sample pore volume is impermeable. Absolute permeability ranges between ~400 to
408 500 mD for sills, decreasing by up to two orders of magnitude for dykes (1 to 275 mD). For
409 all samples, the difference between horizontal and vertical permeability is within the error
410 range of the calculations (Fig. 6). Therefore, no significant permeability directional
411 anisotropy is present (Fig. 6).

412

413 The sample physical properties were also calculated with the pore-filling silica (opal-CT)
414 cement and clay matrix volume digitally removed (CDR). CDR calculations of porosity and
415 permeability range between 28.1-40.8 % (av. 34 %) and 1,200-6,274 mD (av. 3,120 mD),
416 respectively (Table 2; Fig. 6; Supplementary Fig. S4). CDR permeability calculations
417 represent an increase by up to three orders of magnitude in comparison to the cemented case
418 (≤ 1 to ~500 mD) (Fig. 6). The increase of sample permeability is directly proportional to the
419 volume of CDR, which indicates that cement and clay matrix are key controlling factors of
420 sand intrusion porosity and permeability.

421

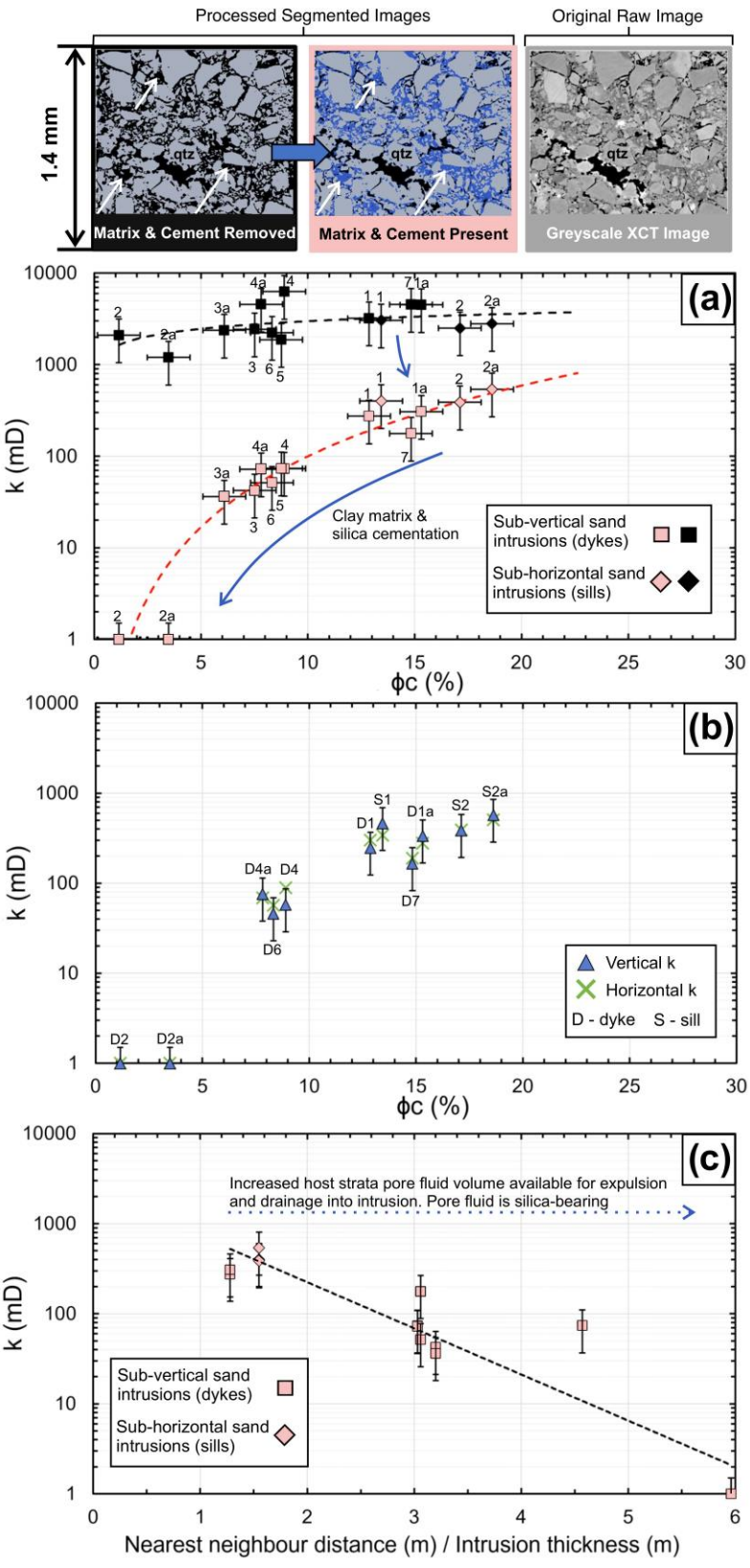

Figure. 6. An assessment of sand intrusion permeability, calculated using µCT image analysis, observing (a) changes caused by cementation, (b) amount of directional anisotropy and (c) correlation to intrusion nearest neighbour distance as a function of thickness. **a)** The mean permeability (k) has been calculated for samples D1-7 and S1-2 with (black) and without (pink) the clay matrix and silica

cement digitally removed. The connected porosity (Φc) for all data points (pink and black) is shown for the cemented case, so the permeability reduction is more clearly visible (see Supplementary Fig. S4 to observe the combined change in porosity-permeability following cement digital removal). Squares - sub-vertical sand intrusions; diamonds - sub-horizontal sand intrusions. **b)** Horizontal and vertical permeability (k) are compared. Vertical k - blue triangles; horizontal k – green crosses. The samples display minimal directionally dependent permeability anisotropy. Samples D3 and D5 are omitted as their in-situ orientation (way-up) is not known. **c)** Plot of permeability and distance to nearest neighbour intrusion as a function of intrusion thickness, with exponential correlation (R^2 - 0.86).

4.3.3 Pore Network Modelling

The pore properties of a dyke sample are determined both with and without CDR, using 3D µCT image data (Fig. 7). For the dyke sample without CDR, pore size diameter ranges from <4-180 μm, with a 70 μm mean pore size. (Fig. 7; Table 2). There is a bimodal pore size frequency distribution (peaks at 55 and 75 μm), with an additional peak below 20 μm, that represents a portion of smaller pores. A comparison of pore size distribution with CDR (Fig. 7), shows that cement and clay matrix infills the modal pore size, indicated by an increased frequency percentage within the 60-80 μm range. In addition, the mean pore connectivity of the dykes increases by a factor of two (4.2 to 9.5), as a result of CDR.

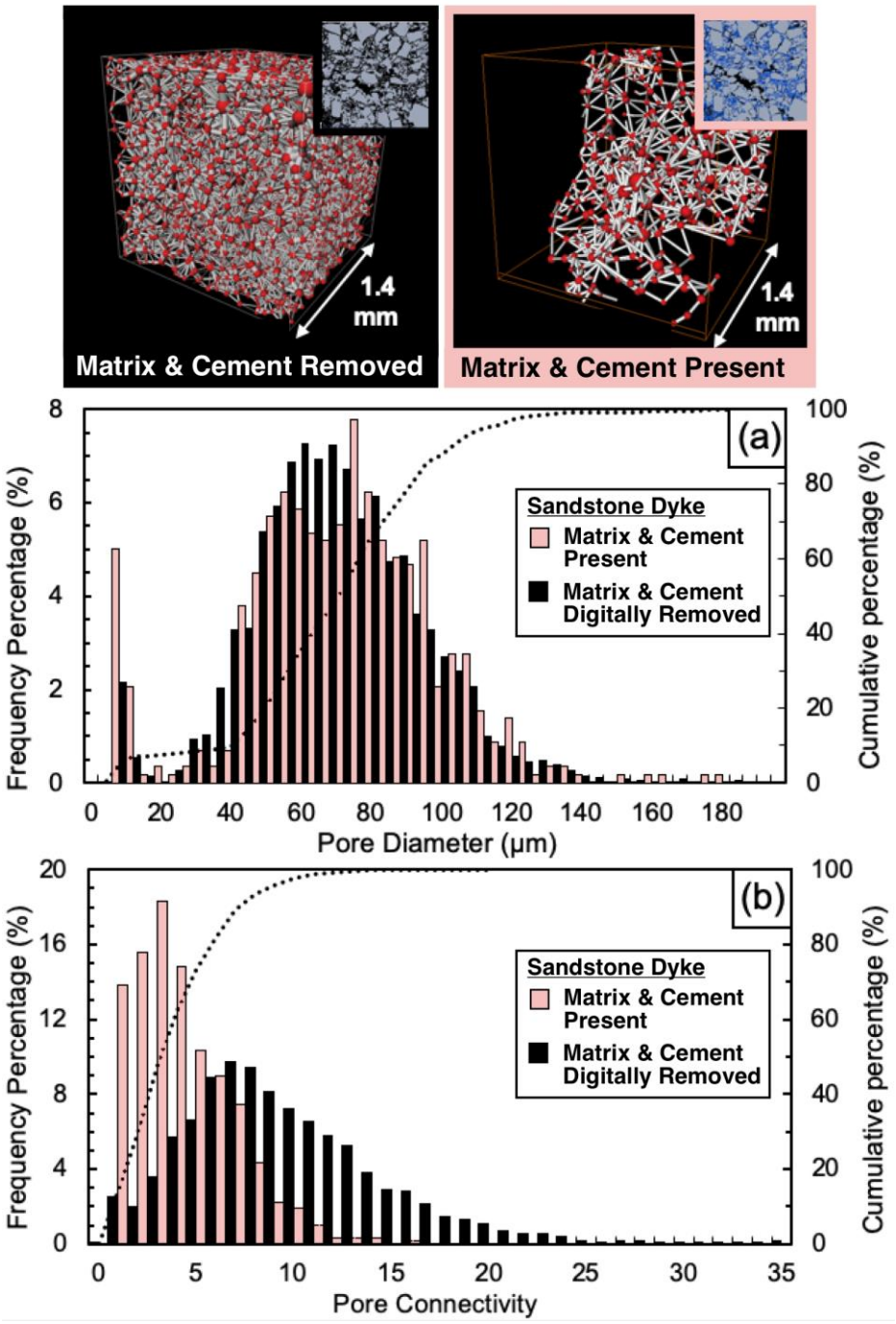

Figure. 7. Pore statistics of a sampled sand intrusion, highlighting the effect of the clay matrix and silica cementation. **A)** A frequency percentage histogram of pore diameter. A comparison with (black) and without (pink) the clay matrix and cement digitally removed suggests that cement infills the modal pore size. **B)** A frequency percentage histogram of pore connectivity. A comparison suggests that clay matrix and silica cementation causes a significant reduction in pore connectivity. 3D Pore network models (PNM) are shown (top and bottom right), derived from the processed 3D X-ray micro CT images, that were used to obtain the pore statistics. The PNMs display throats/pore connections (grey) and pores (red), on a scale that shows relative pore volume size (scale factor of 3.3E-8) and relative throat equivalent radii (scale factor 0.15).

5 Discussion

5.1 Insights from the porosity-permeability data

The 3D µCT method combined with more robust image processing workflows (Callow et al., 2020) provide more accurate and non-invasive physical property calculations, in comparison to conventional 2D studies (Scott et al., 2013) and preliminary insights from 3D analyses (Wu et al., 2017). By subtracting specific mineral features from the calculation, their effect on porosity and permeability could be isolated and quantified. This technique has been applied to obtain minus-cement-and-matrix porosity-permeability values, and to determine the horizontal (k_h) and vertical permeability (k_v) components of each sample.

5.1.1 Comparison of sill and dyke sand intrusions

Mean connected porosities of 8.6 % for dykes and 16.4 % for sills have been calculated. Mean permeability values of 100 mD for high angle dykes and 442 mD for sills have also been calculated. Dyke samples have up to two orders of magnitude lower permeability than sill samples, due to reduced textural maturity (grain microfracturing), as well as increased clay matrix and silica (opal-CT and quartz) cement content (up to 30 % of total sample volume) (Table 1; Figs. 5-6). Scott et al. (2013) used a large sample set of 2D thin sections to calculate connected porosity values of 5-11 % for dykes and 12-19 % for sills, and mean permeability values using a probe permeameter of 81 mD for high angle dykes and 629 mD for sills. These calculations are directly comparable to the results in this study, obtained using the 3D µCT methodology. This highlights that intrusions that are more discordant to host strata bedding, which are less discernable from conventional seismic imaging (Grippa, et al., 2019), commonly have lower porosity and permeability. This key finding has significance for the assessment and modelling of reservoir volume and fluid containment.

5.1.2 Permeability directional anisotropy

The 3D µCT image analysis enabled assessment of the directional anisotropy of permeability. Calculations of kv/kh >1 would indicate enhanced vertical fluid transmissibility. By contrast kv/kh < 1 would indicate increased permeability concordant to bedding, as displayed by a nearby turbiditic sandstone with pristine depositional structures in the Dosados Member (Wu et al., 2017). In this study, kv/kh for sandstone intrusions calculated using µCT imaging are ~1, and within the error of the calculations (Fig. 6b), which suggest very minimal permeability directional anisotropy. The comparison with the depositional sandstone (kv/kh < 1) supports the interpretation of pervasive grain reorganisation due to the action of turbulent flow during sand injection. A previous study of petrographic data from the PGIC was used to determine an average kv/kh = 1.5 for intrusions in PGIC, which supports the interpretation of grain reorganisation and enhanced vertical transmissibility (Scott et al. 2013). Therefore, sand intrusions have a higher vertical permeability relative to depositional sandstones and the surrounding host strata, which highlights their role as sub-vertical fluid-escape structures.

In sandstone intrusions, micro-fractures form by intergranular collisions at high velocity in dilute suspensions (Kleinstreuer, 2010; Hurst et al., 2021a). Using µCT image-based calculations, the minimum fluidisation velocity required for sediment entrainment of the PGIC sandstone intrusions (with average grain sizes of 140 µm) is ~0.01 cm/s (Jonk et al., 2010). Micro-fractured quartz and feldspar grains are characteristic of the studied dyke samples (Fig. 5a-b; Supplementary Fig. S7) and are analogous to those identified in other sandstone intrusions and extrusions (Scott et al., 2009; Bouroullec and Pyles, 2010). However, the micro-fractures stop at individual grain boundaries and present variable orientation, therefore are unlikely to contribute to permeability anisotropy. Micro-fractures may present variable orientation due to the randomly oriented collisions in a dilute particle

suspension during sand injection, as well as further grain reorganisation during sediment burial and compaction.Well developed micro-fractures are also present within nearby Eocene intrusions (>30% micro-fractured grans; Zvirtes et al., 2020).

5.2 Insights from the minus-cement porosity-permeability data

5.2.1 Comparisons with subsurface field data

The novel minus-cement permeability μCT methodology has enabled a closer comparison of outcrop and subsurface data. Clay matrix and silica (opal-CT and quartz) cement have high porosity and low permeability, as they contain a high proportion (60-70 %) of intragranular (unconnected) pores (Callow et al., 2020). The digital removal of clay matrix and cement (CDR) results in porosity-permeability calculations of 28.1-40.8 % and 1,200-6,274 mD for the PGIC outcrop sand intrusions (Table 2; Fig. 6). There are limited available porosity and permeability data from subsurface sandstone intrusions. Core data have been used to derive permeability curves for sandstone intrusions in the Volund field, Norwegian North Sea, showing porosity-permeability values of 30-40 % and 1,000-8,000 mD, respectively (Townsley et al., 2012; Satur et al., 2021). Satur et al. (2021) documented no evidence of significant silica cement or silica diagenesis within the Volund Field. Further, Duranti and Hurst (2004) reported a porosity within the range 30-40% and permeability 1,000-10,000 mD for sandstone intrusions in the Alba Field, Witch Ground Graben, North Sea, obtained from 535 (2.5 cm diameter core plugs) samples. Duranti and Hurst (2004) documented a lack of detrital and authigenic clays (usually < 2%) within the sandstone intrusions of the Alba Field. Therefore, porosity-permeability measurements from both the Volund and Alba fields are closely comparable to calculations of the PGIC outcrop sand intrusions, after digital removal of clay matrix and silica (opal-CT and quartz) cement volume (CDR) (Table 2). Comparable grain sizes, sorting and grain angularity have also been documented between the sandstone

intrusions of the PGIC and the Alba field, which are fine-grained, sub-angular and moderately sorted (Duranti & Hurst, 2004), which further validates the direct comparison of the porosity-permeability calculations.

The PGIC outcrop had an estimated lithostatic gradient of 0.018 MPa m^{-1} and was buried to a maximum depth of 1.5 km (Vigorito and Hurst, 2010), which is comparable to the present-day burial depths and effective stress conditions of the North Sea fields (Hurst et al., 2003a). Sand intrusion formation is a short-lived process of supra-lithostatic pore-fluid pressure (days to weeks; Vigorito and Hurst, 2010). Processes that directly occur after sandstone intrusion formation, such as grain compaction and pore-fluid dewatering, are expected to have occurred for intrusions at both outcrop and subsurface fields. Therefore, mechanical compaction is not considered to be a primary cause for the mismatch between outcrop data (before CDR) and subsurface field data. However, further dewatering will be expected for outcrop data subjected to uplift and exhumation. This may explain the slightly higher permeability ranges present in the Alba Field data (10,000 mD) with respect to the outcrop data (6,274 mD). Therefore, significant differences between the physical properties of sandstone intrusions from outcrop analogue data and subsurface field measurements are primarily attributed to intergranular pore-filling clay matrix and cementation of the PGIC.

5.2.2 Clay matrix and silica cementation processes

The proportion of clay matrix and silica (opal-CT and quartz) cement has been interpreted as a unique characteristic feature of the PGIC outcrop data when compared with North Sea subsurface field data. The clay matrix and silica cementation are compositionally identical to that of the surrounding mudstone host strata (Table 1; Hurst et al., 2021b). Therefore, they are interpreted to be sourced from the host strata (Fig. 8). During sand injection and

557 fluidisation into hydraulic fractures, erosion of the bio-siliceous mudstone host strata occurs,
558 and is reworked by the detachment of angular fragments of the host strata from the margins
559 of fractures during their propagation and filling with fluidised sand (Fig. 8). Spalling of
560 mudstone into fractures continued throughout fluid flow and was likely greatest during the
561 early period of hydraulic fracturing (Zvirtes et al., 2020). Mudstone clasts are present in all
562 samples, and their greater abundance in dyke samples can probably be explained by the
563 increased prevalence of erosional processes for intrusions discordant to bedding (Fig. 5).
564
565 Pore network model analysis has here revealed that the silica (opal-CT and quartz) cement
566 infills the modal sized pores of 55-75 μm diameter (Fig. 7). Given that the presence of silica
567 and clay matrix appears to be independent of pore size, they are interpreted to have become
568 emplaced during the sandstone intrusion formation, derived from spalls of the host strata that
569 were entrained into the intrusion during formation (Fig. 8). Figure 6c highlighted that for
570 increased spacing between dykes, a reduction in the permeability of the dykes occurs, which
571 is attributed to the increased percentage of clay matrix and silica in the intergranular pore
572 volume. This suggests that for more isolated dykes, there is greater entrainment of spalls of
573 host strata into the intrusion. Therefore, if dyke spacing can be quantified from field data, this
574 could improve permeability prediction in sandstone intrusion reservoir models.
575
576 Opal-CT, with minor opal-A, are present and locally abundant within the clay mineral rich
577 host strata of the Tierra Loma and Marca members of the Moreno Fm. (Table 1; Hurst et al.,
578 2021b) and are present in clasts of the host strata introduced into the sandstone intrusions
579 during their emplacement. Clasts derived from the Marca Member are commonly bio
580 siliceous. Physical evidence of the opal-A to -CT transition is preserved as the presence of 3-
581 20 μm sub-spherical crystals formed on diatom tests, displayed using SEM image analysis

582 (Fig. 4), and is evidence that opal-A transitions to opal-CT by a dissolution-reprecipitation
583 reaction. In the reaction, intra-crystalline porosity in opal-A decreases with a concomitant
584 increase in opal density as opal-CT forms and mineral-bound water is expelled, an overall
585 volume loss of the solid phase (Isaacs, 1981). Porosity reduction in the diatomaceous
586 component of the matrix of up to 45 % is expected during the opal-A to opal-CT conversion
587 (Isaacs, 1981; Weller and Behl, 2015). Porosity reduction in diatomaceous mudstone is a
588 combination of the destruction of commonly <1 μm scale micropores in opal-A, crystal
589 growth of coarser opal-CT with visibly less micropores, and mechanical compaction of the
590 coarser opal-CT grains (Fig. 4; Hein et al., 1978; Hurst et al., 2021b). Mudstone from the
591 Tierra Loma and Marca members have generally >12.5% opal-CT (Table 1; Hurst et al.,
592 2021b) so volume reduction is significant where opal-rich clasts are present within the
593 sandstone intrusions (Fig. 5 a, b).
594
595 Escape of water into the aquifer system during the opal-A to -CT transition in bio siliceous
596 mudstone may contribute to sand fluidisation and injection, as pore-fluid expulsion can
597 promote fracture generation within host strata by decreasing effective rock strength. (Davies
598 et al., 2008). Large-scale sand injectites are present within Cenozoic aged biosiliceous
599 sediments from the Northeast Atlantic margin, including the Faeroe-Shetland Basin, the
600 North Viking Graben and the Møre Basin (Davies et al., 2006). Interpretation of seismic
601 surveys from the Faeroe-Shetland Basin reveal seabed pockmarks that overlie probable fluid
602 conduits emanating from intervals with opal-A to opal-CT transition zones (Davies et al.
603 2006). However, direct evidence is lacking for a genetic relationship between sand injection
604 and the opal-A to -CT transition. There is a clear spatial relationship between the PGIC
605 sandstone intrusions and the bio siliceous Marca Member host strata (Fig. 1b). However, all
606 the sandstone intrusions transect the Marca Member rather than emanate from it. Opal-CT is

607 the dominant silica phase present in the Marca Member (Hurst et al., 2021b), however the
608 microstructure retains some characteristics of the progenitor diatoms, which indicates that the
609 Marca Member has been lightly consolidated (Fig. 4). This is similar to the moderate
610 dissolution described in SEM images by Hein et al. (1978) from Cenozoic deposits, believed
611 to record formation in a temperature range from 35˚ to 50˚C, below a >500 m thick
612 overburden of siliceous ooze. With substantially more data, a study by Varkouhi et al. (2021)
613 established a temperature range of <30˚ to >55˚C for the opal-A to -CT transition, noting that
614 active silica diagenesis persists at low (<30˚C) temperature and gives similar diagenetic
615 products, but more slowly, than a more rapid reaction at higher (>55˚C) temperature. Since
616 deposition of the Marca Member (Fig. 1), the SEM analysis suggests that the opal-CT
617 transformation did not reach completion and was predominantly exposed to low temperature,
618 perhaps never much greater than 30˚C. Co-occurrence of abundant fully-expandable di-
619 octahedral smectite (Table 1; Hurst et al., 2021b) supports that silicate transformation
620 typically associated with the 60˚C isotherm (Nadeau, 2011) were not reached, which is
621 supported by previous observations of preserved epidote and calcic amphibole, heavy
622 minerals typically associated with dissolution during early diagenesis (Hurst et al., 2017).
623 Although the effects of volume reduction and textural change in opal-CT rich clasts in
624 sandstone intrusions are observed (Figs 4 and 5), there is no evidence that opal-A to -CT
625 reactions in the host mudstone contributed significant water to sand fluidisation and injection.
626 Therefore, sandstone intrusion formation most likely pre-dated the onset of the opal
627 transition.
628
629 **5.3 Permeability distribution**
630 Integration of the field and µCT data permits an improved understanding of sand intrusion
631 formation processes and temporal evolution. Thinning and bifurcation of dykes upward

occurs in the PGIC (Fig. 3; Vigorito et al., 2008; Vétel and Cartwright, 2010; Vigorito and Hurst, 2010; Grippa et al., 2019) and in the adjacent Eocene Tumey Giant Injection Complex (Zvirtes et al., 2019). A general reduction in fluid transmissivity is inferred upward in giant injection complexes, but despite this, fluid migration through PGIC dykes caused fluid leakage onto the palaeo-seafloor for ~2 Ma, as evidenced by the presence of methane-derived authigenic carbonates (MDAC's) and sandstone extrusions (Minisini and Schwartz, 2007; Blouet et al., 2017). Outcrop observations of individual dykes show subvertical sediment layering and variations in lithification between the sediment layers (Fig. 3). Onlapping of the internal layers, crudely from north to south, reveal less consolidation of individual dykes toward their southern margins. A higher permeability was calculated on the southern side of a dyke D7 (177 mD), relative to its northern side D6 (52 mD) (Fig. 2a, 3c). Southward fracture opening is implied and subsequent filling by later pulses of injected sand (Figs. 2-3; Fig. 8).

Below the Marca Member dykes are commonly >0.5 m across (aperture) (Figs. 2-3) but thin upward in shallower stratigraphic levels (Vigorito et al., 2008; Supplementary Table S1). Approaching the palaeo-seafloor in the Dos Palos Member (Fig. 2), dykes thin and are prone to carbonate cementation (Fig. 3d-g; Fig. 8), which in combination reduce their permeability. Böttner et al. (2021) observed a permeability reduction in sandstone of three orders of magnitude due to carbonate cementation. Pore-filling carbonate cement forms due to the anaerobic oxidation of methane, a process limited to shallow stratigraphic depths; carbonate cement fills pore throats, preventing advective flow upward (Fig. 8). This process occurred above a subsurface sandstone intrusion system in the Gryphon field, North Sea (Mazzini et al., 2003).

These observations highlight the reported conclusion that sandstone dykes not only become less permeable as they thin (Scott et al., 2013), but when layers are present, permeability may vary spatially within them. When considering permeability and networks of sandstone dykes, it is inappropriate to assume homogeneous reservoir quality. In quantitative models of mudstone-dominated seal lithologies, where dykes are present and detected on seismic surveys, they are associated with a higher probability of seal failure (Cartwright et al., 2007). If present, but unresolved, on seismic data, this could have detrimental effects on the prediction of seal effectiveness (Grippa et al., 2019). By integrating pore-scale calculations and field-scale observations, input is provided for a conceptual model that assesses a sand intrusion network's influence on seal effectiveness.

5.3.1 Sand intrusion conceptual model

Integrating the pore- to field-scale observations, a generally applicable model has been developed for sand intrusion formation, and process mechanisms that control sand intrusion permeability, spatially and temporally (Fig. 8):

I. Fluidisation and sand remobilisation from the overpressured parent unit.

II. Sand propagation into hydraulic fractures, erosion (corrasion) of the fine-grained host strata occurs at the fracture margins; fragments and angular spalls of smectite clay and silica are incorporated into the intrusion, and incursion of pore waters occurs from the host strata into the intergranular pore space of the sand intrusion.

III. Post-fluidisation compaction and dewatering of the remobilised sediment, and silica transformation from opal-A (amorphous silica) to opal-CT due to increased pressure-temperature conditions during burial diagenesis. The opal-A to opal-CT transition occurs after the sand intrusion formation, when the whole succession is becoming more deeply buried.

IV. Methane flows upwards through the sand intrusion network, resulting in pore-filling carbonate cementation forming proximal to the palaeo-seafloor by the process of methane-derived anaerobic oxidation.

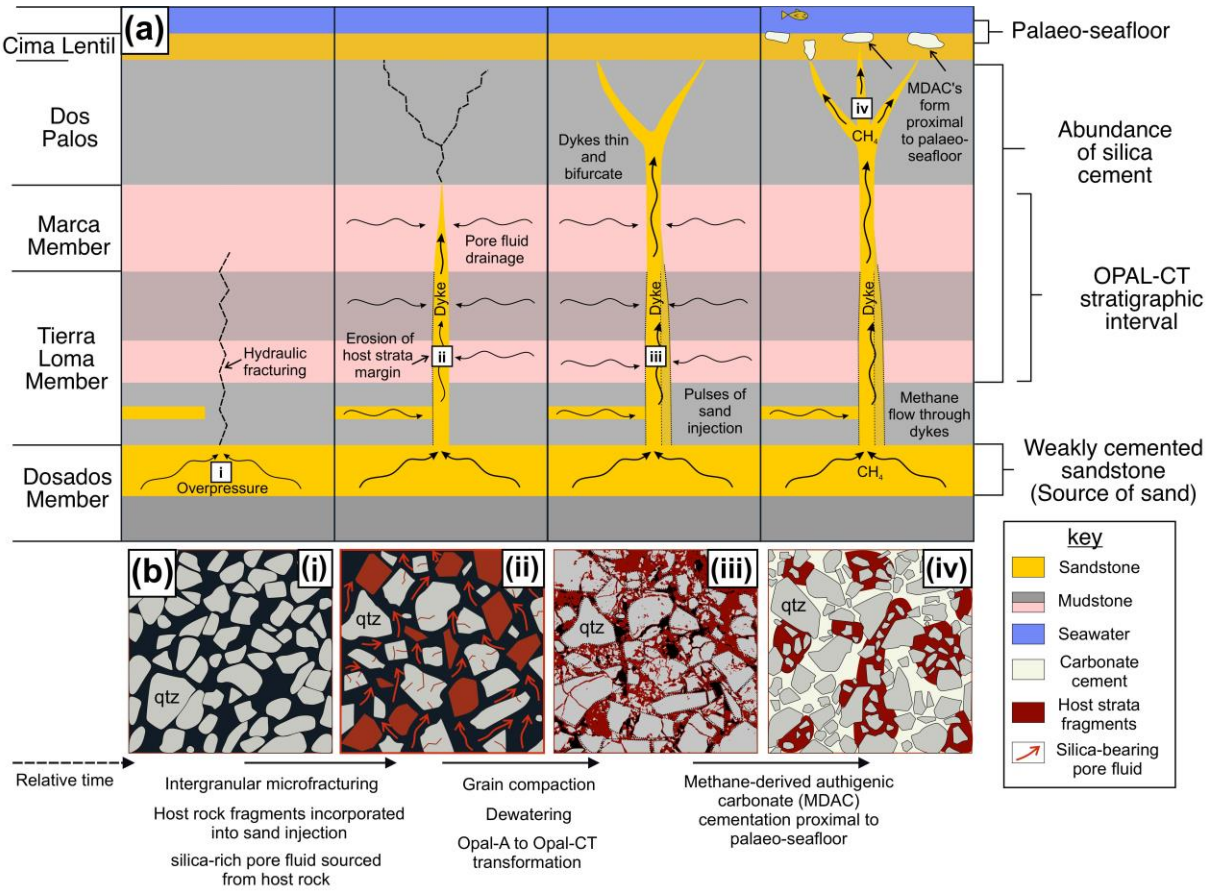

Figure. 8. Conceptual process-based model of a sand intrusion system showing the temporal and spatial evolution of rock texture and pore properties following sand remobilization and intrusion. **a)** The temporal development of sand intrusion formation generates a fluid-escape system which extends vertically upwards to the seafloor through mudstone host strata **b)** Temporal evolution of rock texture and pore properties (i-iv): **i)** Fluidisation and sand remobilisation from overpressured parent units. **ii)** Sand propagates into hydraulic fractures, incorporation of host strata pore waters and erosion-derived clay fragments into the intrusion pore space. **iii)** Post-fluidisation compaction and dewatering of the remobilised sediment; silica transforms from opal-A (amorphous silica) to opal-CT; **iv)** Methane flows upwards through the sand intrusion network; carbonate cementation forms proximal to the seafloor by the process of methane-derived anaerobic oxidation.

Overall, the main difference between the Panoche Hills with respect to the sand intrusion structures in the North Sea and other sedimentary basins worldwide is the proportion of clay matrix and silica (opal-CT and quartz) cement. In the analysis, when the cement is digitally removed from the intergranular pore volume using a novel µCT method approach, porosity-permeability values are closely comparable to those reported for North Sea sand intrusions. This observation supports the validity of the proposed conceptual model to explain fluid-escape systems, both spatially and temporally. Evidence from field observations within Moreno Gulch, Marca Canyon and Escarpados Canyon, suggests that the Panoche Hills represents an ancient fluid-escape system from depth to the palaeo-seabed. The cross-stratal fluid flow within the Panoche Hills extends over a stratigraphic thickness of > 600 m, which is a comparable vertical scale to observations made within sedimentary basins globally, with sediment remobilisation occuring at depth and seep-structures in the near-surface (Fig. 8). Future work should focus on using the findings of the study as a basis for improved process-based fluid simulation and reactive transport models, to understand temporal changes in fluid flux and leakage rates through the sedimentary overburden (Marin-Moreno et al. 2019).

6 Conclusions

This study used a novel minus-cement-and-matrix 3D X-ray micro-CT methodological approach to determine pore- to field-scale permeability heterogeneity of an ancient fluid-escape system, in the Panoche Hills, California. Overall, the study has provided an improved understanding of the controlling mechanisms of permeability heterogeneity and temporal evolution. The main findings of the study are:

1) The Panoche Hills is an exemplar outcrop analogue of a subsurface fluid-escape system, with comparable spatial scales to active systems in offshore, marine sedimentary basins.

2) The presence of silica (opal-CT and quartz) cement and clay matrix within the intergranular pores of sandstone intrusions are the primary control of porosity and permeability spatial heterogeneity (≤ 1 to ~500 mD) within the PGIC outcrop analogue system. The digital removal of clay matrix and silica cement results in more directly comparable calculations to modern, offshore systems (i.e. ~30-40 % porosity and 10^3-10^4 mD permeability) (Fig. 6).
3) Integration of field to pore-scale observations permits the creation of an improved conceptual geological model that constrains fluid-escape system formation processes and temporal evolution (Fig. 8).
4) Overall, the 3D X-ray micro-CT methodology provides improved quantitative comparisons of outcrop analogues with active, offshore systems. This has future application and broad significance for studies of siliciclastic sediments and fluid-escape systems in sedimentary basins, which has implications for hydrocarbon reservoir characterisation, and safe and permanent subsurface carbon storage.

CRediT authorship contribution statement

Author contribution statement: B.C., J.M.B., T.G.: Conceptualization. B.C., I.F.S., S.R.: Formal Analysis. B.C., A.G., A.H., I.F.S.: Validation. B.C.: Data curation, Methodology, Software, Visualization. B.C., J.M.B.: Funding acquisition. B.C., A.G., A.H., I.F.S., J.M.B., S.R., T.G.: Investigation & Writing.

Declaration of Competing Interest

The authors declare that they have no known competing financial interests or personal relationships that could have appeared to influence the work reported in this paper.

Acknowledgements

This work has received funding from the European Union's Horizon 2020 research and innovation programme under grant agreement No.654462 (STEMM-CCS) and the Natural Environment Research Council (CHIMNEY; NE/N016130/1). We also thank the California Bureau of Land Management for facilitating access to the outcrop area. We acknowledge Diamond Light Source (Beamline I13–2; MT18758). We thank Sharif Ahmed, Hans Deyhle, Hector Marin-Moreno, Laurence North, Christina Reinhard, Shashi Marathe, Kaz Wanelik, Andrew Bodey, Matthew Beverley-Smith, Daniel Doran, Richard Pearce and the Diamond Support Scientists at I13–2 for their support. We acknowledge the use of the IRIDIS High Performance Computing Facility, μ-VIS X-Ray Imaging Centre, and the scanning electron microscope (SEM) facility at the University of Southampton. We acknowledge and thank the British Ocean Sediment Core Research Facility (BOSCORF). We also thank the FEI Visualization Sciences Group for providing the use of the Avizo 9.3.0 software for μCT image processing. Finally, we would like to sincerely thank Richard H. Worden and Thomas Seers for their constructive comments, which greatly improved the manuscript. The data set associated with this work is available online at https://doi.org/10.5258/SOTON/D1441. Here we provide the raw and segmented μCT tomographic image data, and the associated image processing files.

Six supplementary figures (Figs. S1-S6) and one supplementary table (Table S1) are provided for this article.

References

Alansari, A., Salim, A.M.A., Janjuhah, H.T., Bin Abd Rahman, A.H., Fello, N.M., 2019. Quantification of clay mineral microporosity and its application to water saturation and effective porosity estimation: a case study from Upper Ordovician reservoir, Libya. Journal of Natural Gas Geoscience, 4, 139–150.

Arganda-Carreras, I., Kaynig, V., Rueden, C., Eliceiri, K.W., Schindelin, J., Cardona, A., Seung, H.S., 2017. Trainable Weka segmentation: a machine learning tool for microscopy pixel classification, Bioinformatics, 33, 2424–2426.

Andresen, K.J., 2012. Fluid flow features in hydrocarbon plumbing systems: What do they tell us about the basin evolution?. Marine Geology, 332, 89-108, doi: 10.1016/j.margeo.2012.07.006.Avizo, 2018. Avizo 3D Software User's Guide. FEI. https://www.fei.com/software/avizo-user-guide/ (accessed 02.10.2019).

Bartow, J.A., 1996. Geologic map of the west border of the San Joaquin Valley in the Panoche Creek-Cantua Creek area, Fresno and San Benito counties, California. US Geological Survey Miscellaneous Geologic Investigations Map I-2430.

Blouet, J.P., Imbert, P., Foubert, A., 2017. Mechanisms of biogenic gas migration revealed by seep carbonate paragenesis, Panoche Hills, California. AAPG Bulletin, 101, 1309-1340, doi: 10.1306/10171616021.

Bodey, A.J., Rau, C., 2017. Launch of the I13-2 data beamline at the Diamond Light Source synchrotron. Journal of Physics: Conference Series, 849, 012038, doi: 10.1088/1742-6596/849/1/012038.

Böttner, C., Callow, B.J., Schramm, B., Gross, F., Geersen, J., Schmidt, M., Vasilev, A., Petsinski, P., Berndt, C., 2021. Focused methane migration formed pipe structures in permeable sandstones: Insights from uncrewed aerial vehicle-based digital outcrop analysis in Varna, Bulgaria. Sedimentology, 68(6), 2765-2782, doi: 10.1111/sed.12871.

795 Bouroullec, R., Pyles, D.R., 2010. Sandstone extrusions and slope channel architecture and
796 evolution: Mio-Pliocene Monterey and Capistrano Formations, Dana Point Harbor, Orange
797 County, California, USA. Journal of Sedimentary Research, 80(5), 376-392, doi:
798 10.2110/jsr.2010.043.

799 Briedis, N.A., Bergslien, D., Hjellbakk, A., Hill, R.E., Moir, G.J., 2007. Recognition Criteria,
800 Significance to Field Performance, and Reservoir Modeling of Sand Injections in the Balder
801 Field, North Sea. In: Hurst, A., Cartwright, J., Eds., Sand injectites: Implications for
802 hydrocarbon exploration and production, AAPG Memoir, 87, 91-102.

803 Callow, B., Falcon-Suarez, I., Marin-Moreno, H., Bull, J.M., Ahmed, S., 2020. Optimal X-ray
804 micro-CT image based methods for quantification of porosity and permeability in
805 heterogeneous sandstone. Geophysical Journal International, 223(2), 1210-1229,
806 doi:10.1093/gji/ggaa321.

807 Cartwright, J., Huuse, M., Aplin, A., 2007. Seal bypass systems. AAPG bulletin, 91, 1141-1166,
808 doi: 10.1306/04090705181.

809 Cobain, S.L., Peakall, J., Hodgson, D.M., 2015. Indicators of propagation direction and relative
810 depth in clastic injectites: Implications for laminar versus turbulent flow processes.
811 Geological Society of America Bulletin, 127, 1816-1830, doi: 10.1130/B31209.1.

812 Davies, R.J., Goulty, N.R., Meadows, D., 2008. Fluid flow due to the advance of basin-scale
813 silica reaction zones. Geological Society of America Bulletin, 120, 195-206, doi:
814 10.1130/B26099.1.

815 Davies, R.J., Huuse, M., Hirst, P., Cartwright, J., Yang, Y., 2006. Giant clastic intrusions
816 primed by silica diagenesis. Geology, 34, doi: 10.1130/G22937A.1.

817 Duranti, D., Hurst, A., 2004. Fluidization and injection in the deep-water sandstones of the
818 Eocene Alba Formation (UK North Sea). Sedimentology, 51, 503-529, doi: 10.1111/j.1365-
819 3091.2004.00634.

820 Duranti, D., Hurst, A., Bell, C., Groves, S., 2002. Injected And Remobilised Sands Of The Alba
821 Field (Ukcs): Sedimentary Facies Characteristics And Wireline Log Responses. Petroleum
822 Geoscience 8, 99-107, do: 10.1144/petgeo.8.2.99.

823 Etiope, G., Ciotoli, G., Schwietzke, S., Schoell, M., 2019. Gridded maps of geological methane
824 emissions and their isotopic signature. Earth System Science Data, 11, 1-22, doi:
825 10.5194/essd-11-1-2019.

826 Falcon-Suarez, I.H., North, L., Callow, B., Bayrakci, G., Bull, J., Best, A., 2020. Experimental
827 assessment of the stress-sensitivity of combined elastic and electrical anisotropy in shallow
828 reservoir sandstones. Geophysics, 85(5), MR271-MR283, doi: 10.1190/geo2019-0612.1.

829 Foschi, M., Cartwright, J.A., MacMinn, C.W., Etiope, G., 2020. Evidence for massive emission
830 of methane from a deep-water gas field during the Pliocene. Proceedings of the National
831 Academy of Sciences, 117(45), 27869-27876, doi: 10.1073/pnas.2001904117.

832 Gera, D., Syamlal, M., O'Brien, T.J., 2004. Hydrodynamics of particle segregation in fluidized
833 beds. International Journal of Multiphase Flow, 30, 419-428, doi:
834 10.1016/j.ijmultiphaseflow.2004.01.003.

835 Greinert, J., McGinnis, D.F., Naudts, L., Linke, P., De Batist, M., 2010. Atmospheric methane
836 flux from bubbling seeps: Spatially extrapolated quantification from a Black Sea shelf area.
837 Journal of Geophysical Research: Oceans, 115 (C1), doi: 10.1029/2009JC005381.

838 Grippa, A., Hurst, A., Palladino, G., Iacopini, D., Lecomte, I., Huuse, M., 2019. Seismic
839 imaging of complex geometry: Forward modeling of sandstone intrusions. Earth and
840 Planetary Science Letters, 513, 51-63, doi: 10.1016/j.epsl.2019.02.011.

841 Hein, J.R., Scholl, D.W., Barron, J.A., Jones, M.G., Miller, J., 1978. Diagenesis of late
842 Cenozoic diatomaceous deposits and formation of the bottom simulating reflector in the
843 southern Bering Sea. Sedimentology, 25(2), 155-181, doi: 10.1111/j.1365-
844 3091.1978.tb00307.x.

845 Hurst, A., Luzinski, W., Zvirtes. G., Vigorito, M., Scott, A., Morton, A.C., Wu, F., 2021a.
846 Diagnostic petrographic and mineralogical criteria for identifying sandstone intrusions. In:
847 Subsurface Sand Remobilization and Injection: Implications for Oil and Gas Exploration
848 and Development eds. Silcock, S., Huuse, M., Bowman, M., Hurst, A. and Cobain, S.
849 Geological Society of London Special Publications, 493, 287-302,
850 https://doi.org/10.1144/SP493-2018-063.

851 Hurst, A., Cartwright, J.A., Huuse, M., Jonk, R., Schwab, A.M., Duranti, D., Cronin, B.T.,
852 2003a. Significance Of Large-Scale Sand Injectites As Long-Term Fluid Conduits:
853 Evidence From Seismic Data. Geofluids 3, 263-274, doi: 10.1046/j.1468-
854 8123.2003.00066.x.

855 Hurst, A. Cartwright, J.A., Duranti, D., 2003b. Fluidisation Structures In Sandstone Produced
856 By Upward Injection Through A Sealing Lithology. In: Van Rensbergen, P., Hillis, R.R.,
857 Maltman, A.J., Morley, C.K., Eds, Subsurface Sediment Mobilization. Geological Society,
858 London, Special Publications, 216, 123-137, doi: 10.1144/GSL.SP.2003.216.01.09.

859 Hurst, A., Scott, A., Vigorito, M., 2011. Physical characteristics of sand injectites. Earth-
860 Science Reviews, 106(3-4), 215-246. doi: 10.1016/j.earscirev.2011.02.004.

861 Hurst, A., Morton, A., Scott, A., Vigorito, M., Frei, D., 2017. Heavy-mineral assemblages in
862 sandstone intrusions: panoche giant injection complex, California, USA. Journal of
863 Sedimentary Research, 87, 388-405, doi: 10.2110/jsr.2017.22.

Hurst, A., Nadeau, P.H., 1995. Clay microporosity in reservoir sandstones—an application of quantitative electron-microscopy in petrophysical evaluation. AAPG Bulletin-American Association of Petroleum Geologists, 79, 563–573.Hurst, A., Wilson, M.J., Grippa, A, Wilson, L., Palladino, G., Belviso, C., Cavalcante, F., 2021b. Provenance and Sedimentary Context of Clay Mineralogy in an Evolving Forearc Basin, Upper Cretaceous-Paleogene and Eocene Mudstones, San Joaquin Valley, California. Minerals, 11(1), 71. doi: 10.3390/min11010071.

Huuse, M., Cartwright, J., Hurst, A., Steinsland, N., 2007. Seismic characterization of large-scale sandstone intrusions. In: Hurst, A., Cartwright, J., Eds., Sand injectites: Implications for hydrocarbon exploration and production, AAPG Memoir, 87, 21–35, doi: 10.1306/1209847M873253.

Ingersoll, R.V., 1979. Evolution of the Late Cretaceous forearc basin, northern and central California. Geological Society of America Bulletin, 90, 813, doi: 10.1130/0016-7606(1979)90<813:EOTLCF>2.0.CO;2.

Ingersoll, R.V., 2019. Subduction-related sedimentary basins of the US Cordillera. In: Miall, A.D., Eds., The sedimentary basins of the United States and Canada, 477-510. doi: 10.1016/B978-0-444-63895-3.00011-5.

Isaacs, C.M., 1981. Porosity reduction during diagenesis of the Monterey Formation, Santa Barbara coastal area, California. In: Garrison, R.E., Douglas, R.G., Eds., The Monterey Formation and Related Siliceous Rocks of California: Society of Economic Paleontologists and Mineralogists, Pacific Section, 257– 271.

Jonk, R., 2010. Sand-rich injectites in the context of short-lived and long-lived fluid flow. Basin Research, 22, 603-621, doi: 10.1111/j.1365-2117.2010.00471.x.

887 Judd, A., Hovland, M., 2009. Seabed fluid flow: the impact on geology, biology and the marine
888 environment. Cambridge University Press, doi: 10.1017/CBO9780511535918.

889 Karstens, J., Ahmed, W., Berndt, C., Class, H., 2017. Focused fluid flow and the sub-seabed
890 storage of CO2: Evaluating the leakage potential of seismic chimney structures for the
891 Sleipner CO2 storage operation. Marine and Petroleum Geology, 88, 81-93, doi:
892 10.1016/j.marpetgeo.2017.08.003.

893 Karstens, J., Berndt, C., 2015. Seismic chimneys in the Southern Viking Graben – Implications
894 for palaeo fluid migration and overpressure evolution. Earth and Planetary Science Letters,
895 412, 88-100, doi: 10.1016/j.epsl.2014.12.017.

896 Ketcham, R.A., Carlson, W.D., 2001. Acquisition, optimization and interpretation of X-ray
897 computed tomographic imagery: applications to the geosciences. Computers &
898 Geosciences, 27, 381-400, doi: 10.1016/S0098-3004(00)00116-3.

899 Kleinstreuer C., 2010. Dilute Particle Suspensions. In: Modern Fluid Dynamics. Fluid
900 Mechanics and Its Applications, 87. Springer, Dordrecht, doi: 10.1007/978-1-4020-8670-
901 0_6.

902 Leifer, I., Boles, J., 2005. Measurement of marine hydrocarbon seep flow through fractured
903 rock and unconsolidated sediment. Marine and Petroleum Geology, 22(4), 551-568, doi:
904 10.1016/j.marpetgeo.2004.10.026

905 Lonergan, L., Borlandelli, C., Taylor, A., Quine, M., Flanagan, K., 2007. The three-dimensional
906 geometry of sandstone injection complexes in the Gryphon Field, United Kingdom North
907 Sea. In: Hurst, A., Cartwright, J., Eds., Sand injectites: Implications for hydrocarbon
908 exploration and production, AAPG Memoir, 87, 103-112, doi:10.1306/1209854M873260.

909 Løseth, H., Gading, M., Wensaas, L., 2009. Hydrocarbon leakage interpreted on seismic data.
910 Marine and Petroleum Geology, 26(7), 1304-1319, doi: 10.1016/j.marpetgeo.2008.09.008.

911 Marin-Moreno, H., Bull J. M., Matter J., Sanderson, D. J. & Roche, B., 2019. Reactive transport
912 modelling insights into CO_2 migration through sub-vertical fluid flow structures.
913 International Journal of Greenhouse Gas Control, 86, 82-92, doi:
914 10.1016/j.ijggc.2019.04.018.
915 Mazzini, A., Duranti, D., Jonk, R., Parnell, J., Cronin, B.T., Hurst, A., Quine, M., 2003. Palaeo-
916 carbonate seep structures above an oil reservoir, Gryphon Field, Tertiary, North Sea. Geo-
917 Marine Letters, 23(3-4), 323-339, doi: 10.1007/s00367-003-0145-y.
918 Minisini, D., Schwartz, H., 2007. An early Paleocene cold seep system in the Panoche and
919 Tumey Hills, central California (United States). In: Hurst, A., Cartwright, J., Eds., Sand
920 injectites: Implications for hydrocarbon exploration and production, AAPG Memoir, 87,
921 185– 197, doi: 10.1306/1209862M873264.
922 Nadeau, P.H., 2011. Earth's energy ''Golden Zone'': a synthesis from mineralogical research.
923 Clay Minerals, 46, 1–24, doi: 10.1180/claymin.2011.046.1.1.
924 Ravier, E., Guiraud, M., Guillien, A., Vennin, E., Buoncristiani, J.-F., Portier, E., 2015. Micro-
925 to macro-scale internal structures, diagenesis and petrophysical evolution of injectite
926 networks in the Vocontian Basin (France): Implications for fluid flow. Marine and
927 Petroleum Geology, 64, 125-151, doi: 10.1016/j.marpetgeo.2015.02.040.
928 Ross, J.A., Peakall, J., Keevil, G.M., 2014. Facies and flow regimes of sandstone-hosted
929 columnar intrusions: Insights from the pipes of Kodachrome Basin State Park.
930 Sedimentology, 61(6), 1764-1792. doi: 10.1111/sed.12115.
931 Satur, N., Hurst, A., Bang, A., Skjærpe, I., Muehlboeck, S.A. 2021. Characteristics of an
932 injection wing, Volund Field. In: Subsurface Sand Remobilization and Injection:
933 Implications for Oil and Gas Exploration and Development eds, Silcock, S., Huuse, M.,

934 Bowman, M., Hurst, A. and Cobain, S. Geological Society of London Special Publications,
935 493, 151-166, doi.org/10.1144/SP493-2017-309.

936 Saunois, M., Stavert, A.R., Poulter, B., Bousquet, P., Canadell, J.G., Jackson, R.B., Raymond,
937 P.A., Dlugokencky, E.J., Houweling, S., Patra, P.K., Ciais, P., ...& Zhuang, Q., 2020. The
938 Global Methane Budget 2000–2017, Earth System Science Data, 12, 1561-1623, doi:
939 10.5194/essd-12-1561-2020.

940 Scott, A., Hurst, A., Vigorito, M., 2013. Outcrop-based reservoir characterization of a
941 kilometer-scale sand-injectite complex. AAPG Bulletin, 97, 309-343, doi:
942 10.1306/05141211184.

943 Scott, A., Vigorito, M., Hurst, A., 2009. The Process of Sand Injection: Internal Structures and
944 Relationships with Host Strata (Yellowbank Creek Injectite Complex, California, U.S.A.).
945 Journal of Sedimentary Research, 79, 568-583, doi: 10.2110/jsr.2009.062.

946 Shakhova, N., Semiletov, I., Salyuk, A., Yusupov, V., Kosmach, D., Gustafsson, Ö., 2010.
947 Extensive methane venting to the atmosphere from sediments of the East Siberian Arctic
948 Shelf. Science, 327 (5970), 1246-1250, doi: 10.1126/science.1182221.

949 Townsley, A., Schwab, A.M., Jameson, E.W., 2012. The Volund Field: developing a unique
950 sand injection complex in Offshore Norway. Paper SPE 154912, SPE Europec/EAGE
951 Conference, Copenhagen, June, https://doi.org/10.2118/154912-MS.

952 Varkouhi, S., Tosca, N.J., Cartwright, J.A., 2021. Temperature–time relationships and their
953 implications for thermal history and modelling of silica diagenesis in deep-sea sediments.
954 Marine Geology, 439, 106541, doi: 10.1016/j.margeo.2021.106541.

955 Vétel, W., Cartwright, J., 2010. Emplacement mechanics of sandstone intrusions: insights from
956 the Panoche Giant Injection Complex, California. Basin Research, 22(5), 783-807. doi:
957 10.1111/j.1365-2117.2009.00439.x

Vigorito, M., Hurst, A., 2010. Regional sand injectite architecture as a record of pore-pressure evolution and sand redistribution in the shallow crust: insights from the Panoche Giant Injection Complex, California. Journal of the Geological Society, 167, 889-904, doi: 10.1144/0016-76492010-004.

Vigorito, M., Hurst, A., Cartwright, J., Scott, A., 2008. Regional-scale shallow crustal remobilization: processes and architecture. Journal of the Geological Society, 165, 609-612, doi: 10.1144/0016-76492007-096.

Weller, R., Behl, R.J., 2015. Physical and Mechanical Characteristics of the Opal-A to Opal-CT Transition Zone: Enhanced Diatomite Permeability from Heterogeneous Diagenetic Embrittlement: Oxnard, California, Pacific Section of American Association of Petroleum Geologists, Society of Economic Geologists, and Society for Sedimentary Geology, Joint Technical Conference, 51112.

Wu, F., Hurst, A., Grippa, A., 2017. Grain and pore microtexture in sandstone sill and depositional sandstone reservoirs: preliminary insights. Petroleum Geoscience, 24, 236-243, doi: 10.1144/petgeo2017-027.

Zvirtes, G., Philipp, R.P., Hurst, A., Palladino, G., De Ros, L.F., Grippa, A., 2020. Petrofacies of Eocene sand injectites of the Tumey Giant Injection Complex, California (USA). Sedimentary Geology, 400, 105617, doi: 10.1016/j.sedgeo.2020.105617.

Appendix A. Supplementary Material

Six supplementary figures (Figs. S1-S7) and two supplementary tables (Table S1-S2) are provided for this article.

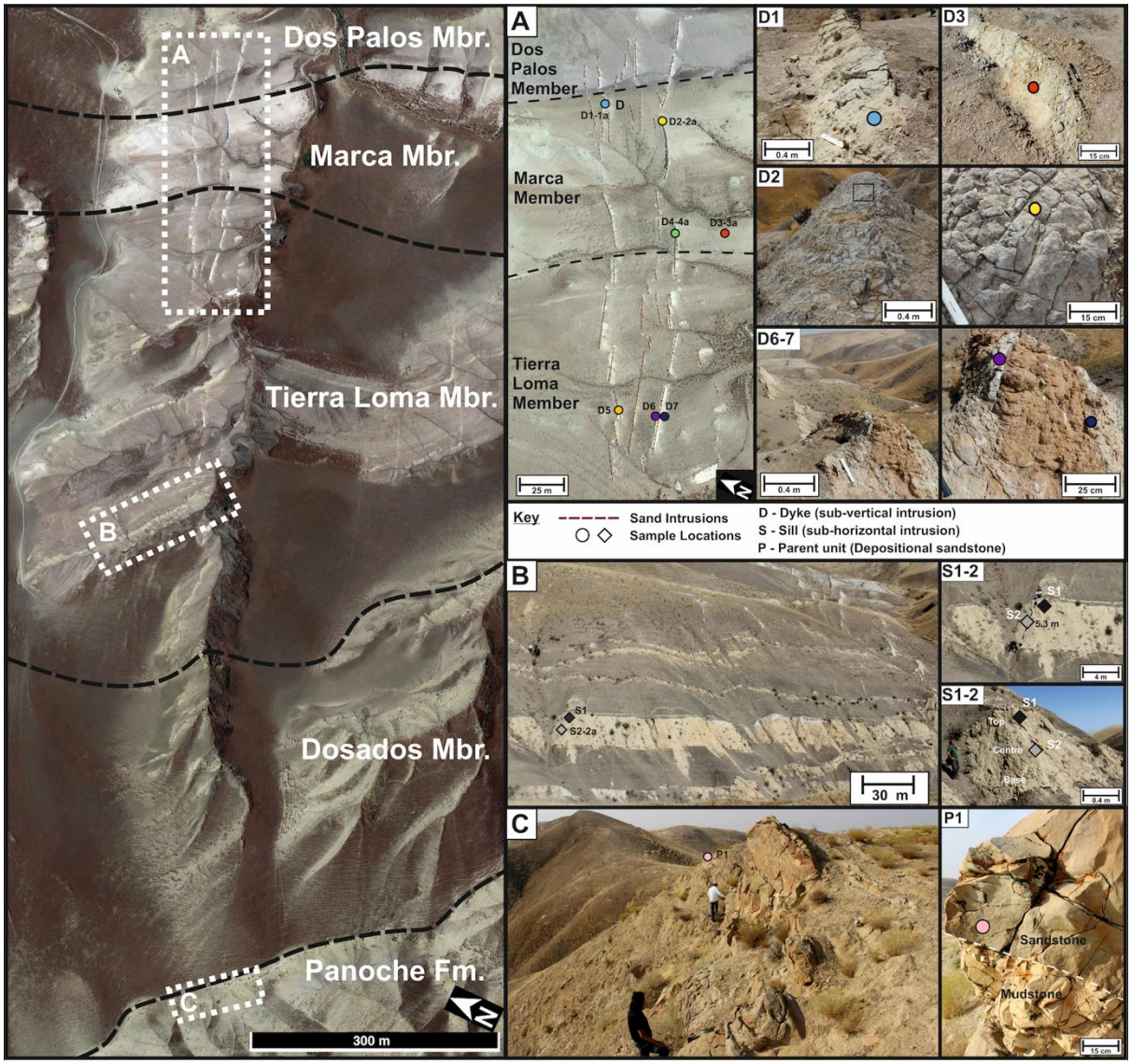

Supplementary Figure. S1. Sand intrusion sampling locations, collected in Moreno Gulch, Panoche Hills. The Google Earth satellite map (left) displays the three primary sampling locations within Moreno Gulch: A) The upper dyke zone; B) The sill zone and C) A sample locality of a depositional (parent) sandstone unit. Individual sampling locations of dykes (D1-D7) and sills (S1-S2) are indicated with coloured circles.

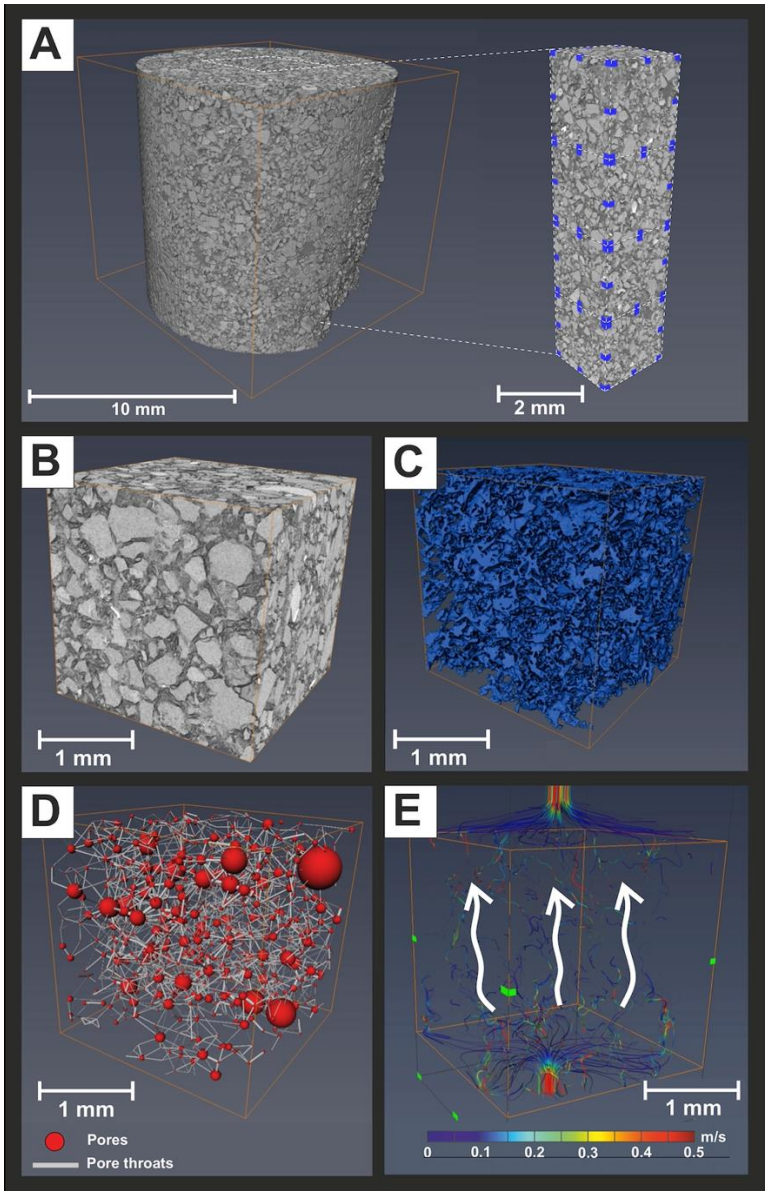

Supplementary Figure. S2. A summary of the 3D X-ray micro-CT image processing and analysis used in this study. **A)** A 1.4 mm cubic length subvolume/region of interest (ROI) is acquired from the full sample volume. A cube of length 1.4 mm (using an image resolution of 0.81 um) has been determined to be a representative elementary volume (REV) for the calculation of porosity and permeability for heterogeneous sandstone samples (Callow et al., 2020). **B)** The cropped ROI is segmented, whereby **C)** the connected pore phase is isolated and characterised - shown in blue. During the segmentation process, five phases could be accurately distinguished: 1) Air; 2) solid grains (that include quartz feldspar, lithic grains and heavy minerals); 3) clay matrix and silica (Opal-CT and quartz) cement and; 4) carbonate cement. Therefore, pore properties could be quantified with and without the clay matrix and cement digitally removed. **D)** A pore network model could be created from the connected pore volumes, allowing individual pores (pink) and throats/pore connections (grey) to be separated and quantified. The pores and throats are displayed on a scale that shows relative pore volume size (scale factor of 3.3E-8) and relative throat equivalent radii (scale factor 0.15). **E)** Image-based finite element modelling (FEM) was used to calculate the absolute permeability of the sample pore volumes using a Navier-stokes flow solver (Avizo).

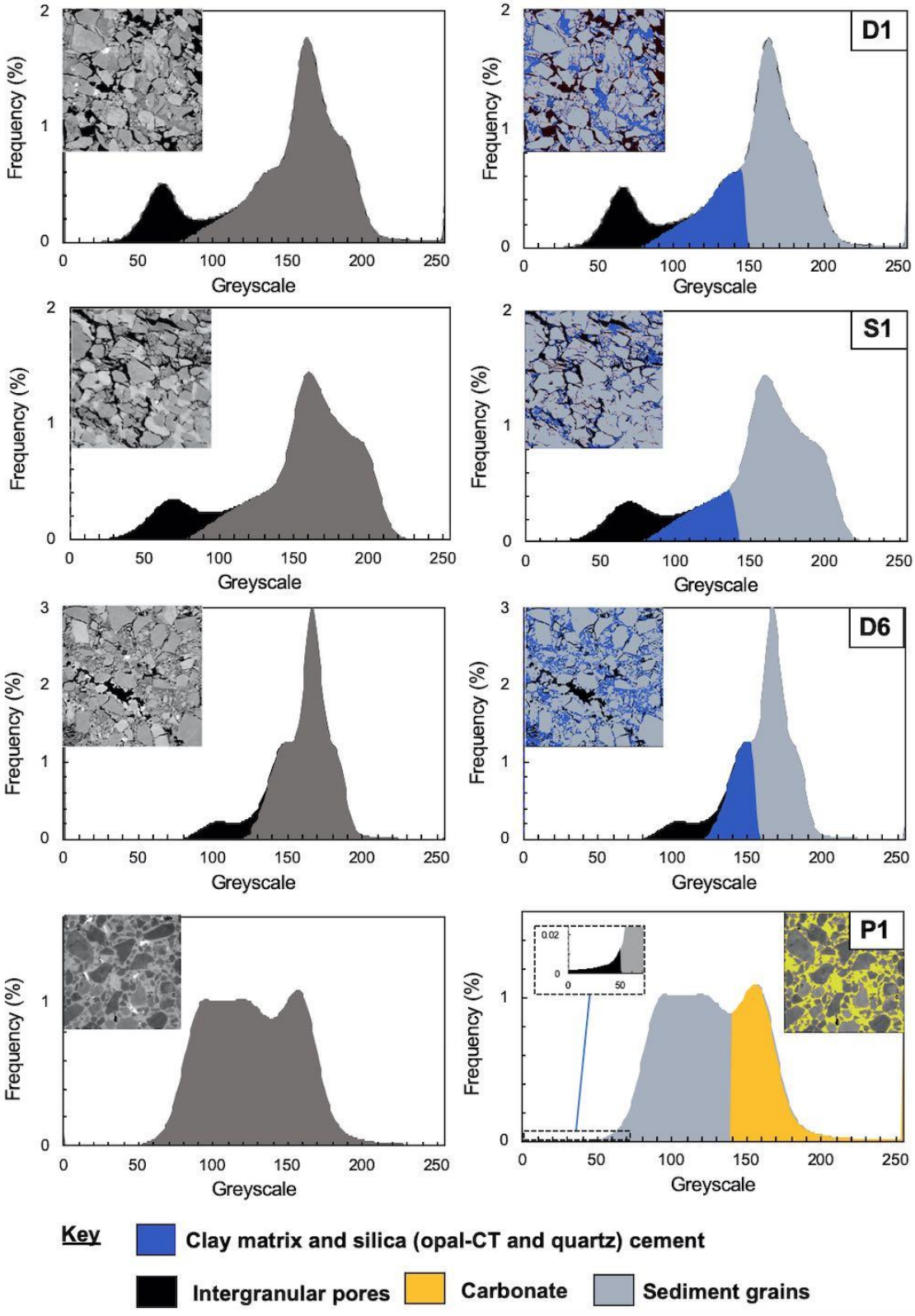

Supplementary Figure. S3. Greyscale intensity curves, highlighting the segmentation and distinction of different phases during 3D x-ray micro-CT image processing. The following phases could be accurately distinguished: 1) Intergranular pores (air) - black; 2) solid grains (that include quartz feldspar, lithic grains and heavy minerals) - light grey; 3) clay matrix - red; 4) silica (Opal-CT and quartz) cement - blue and; 5) carbonate cement - yellow.

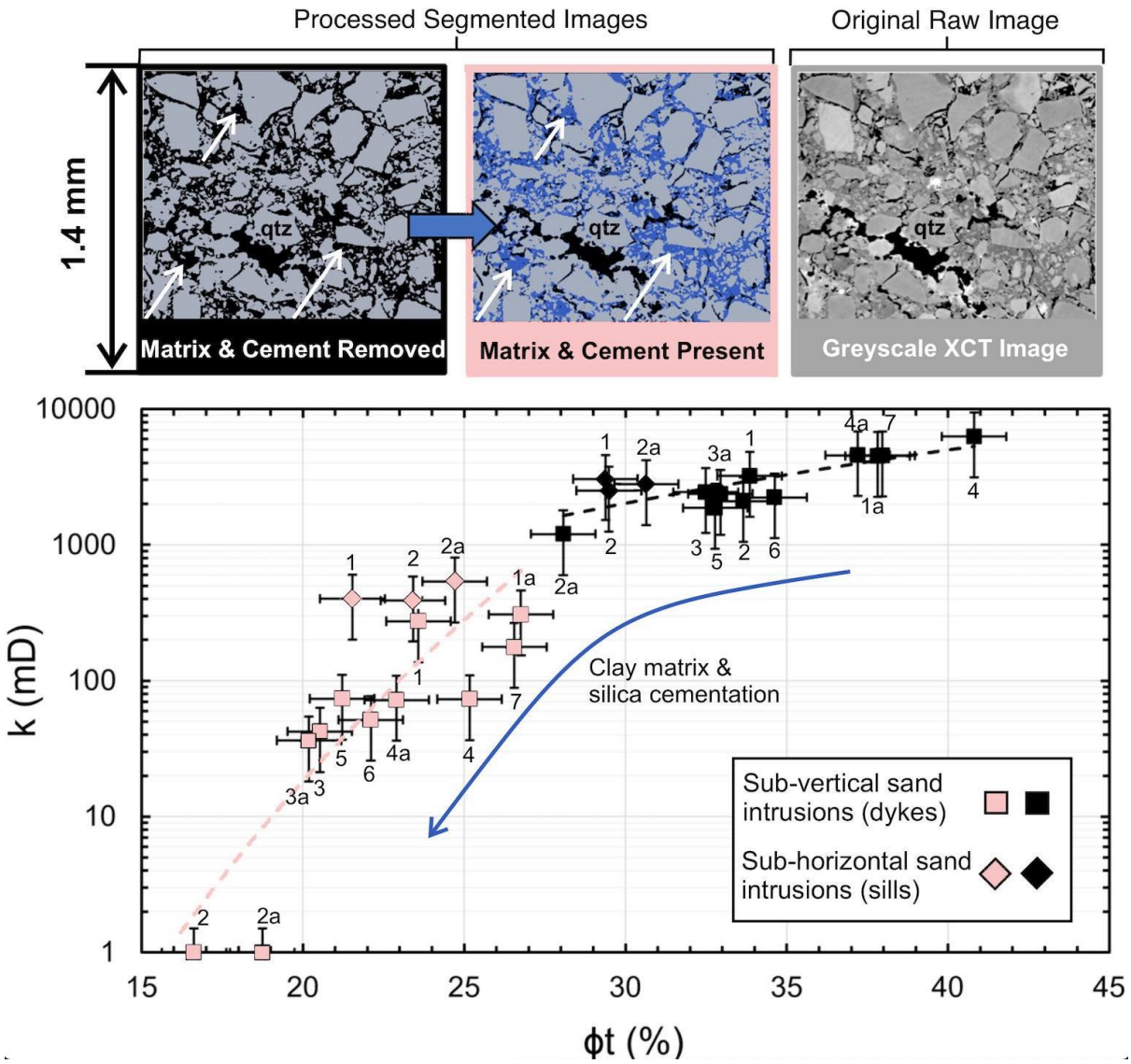

Supplementary Figure. S4. Porosity-permeability plot, highlighting the porosity and permeability reduction caused by clay matrix and silica (Opal-CT and quartz) cementation. The total porosity and permeability have been calculated for samples D1-7 and S1-2 with (black) and without (pink) the clay matrix and cement digitally removed. Circles - sub-vertical sand intrusions (dykes); diamonds - sub-horizontal sand intrusions (sills).

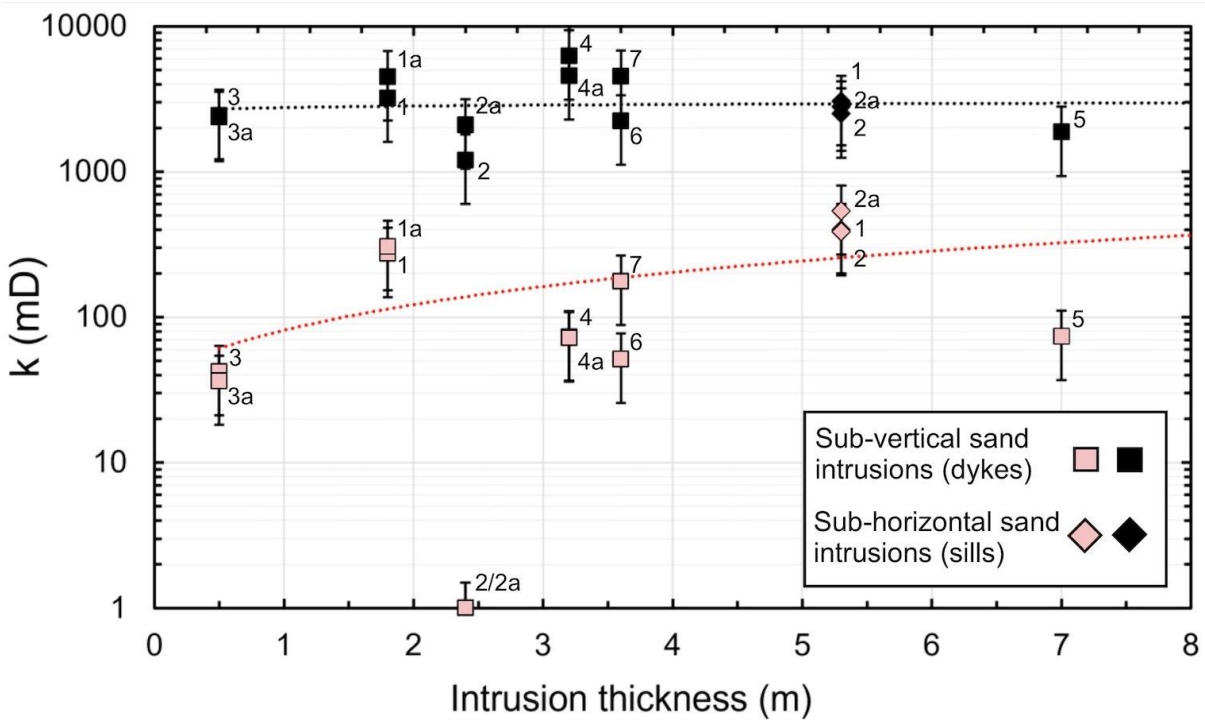

Supplementary Figure. S5. A plot of sand intrusion permeability vs intrusion thickness. The permeability has been calculated for samples D1-7 and S1-2 with (black) and without (pink) the clay matrix and cement digitally removed. Overall there is a weak positive correlation (R^2 - 0.19) between intrusion thickness and permeability. However, the number of samples may be a limiting factor.

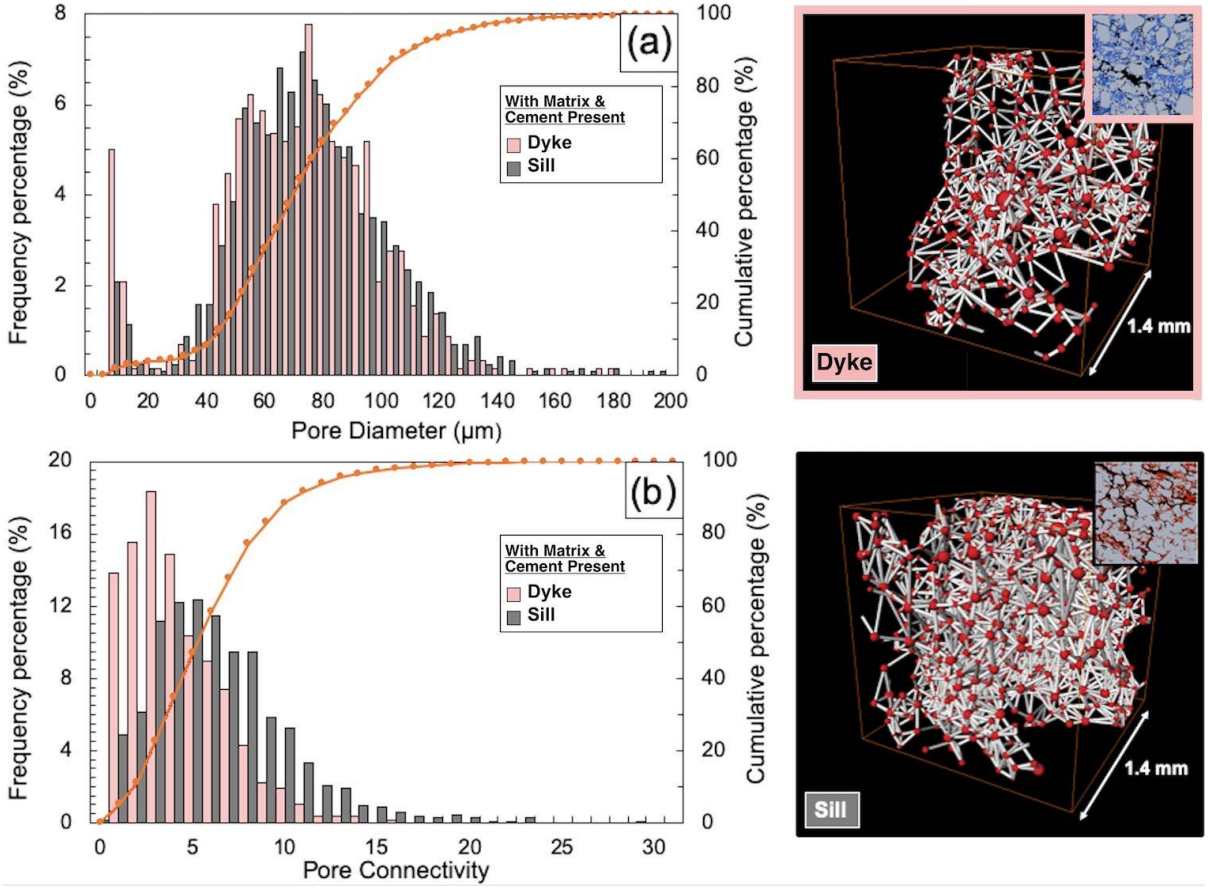

Supplementary Figure. S6. Pore statistics of sampled sand intrusions provides a comparison between a silica cemented dyke (pink) and a sill (grey). **A)** A frequency percentage histogram of pore diameter. A comparison shows that the sill has a more unimodal pore size distribution and a lower proportion of pores below 20 µm. **B)** A frequency percentage histogram of pore connectivity. A comparison shows that the sill has greater pore connectivity than the cemented dyke. 3D Pore network models (PNM) are shown (top and bottom right), derived from the processed 3D X-ray micro CT images used to obtain the pore statistics. The PNMs display throats/pore connections (grey) and pores (pink), on a scale that shows relative pore volume size (scale factor of 3.3E-8) and relative throat equivalent radii (scale factor 0.15).

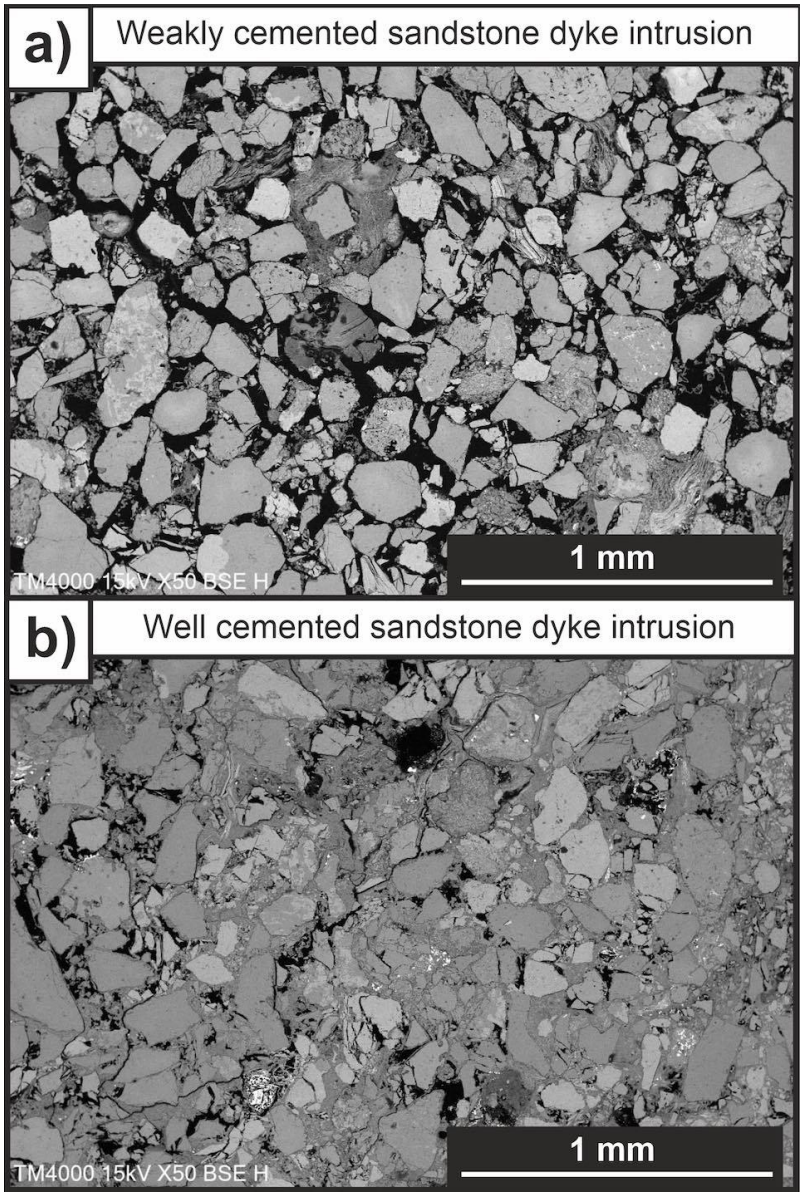

Supplementary Figure. S7. Scanning Electron microscopy images displaying the textural and compositional variability of sandstone intrusions. a-b) Displayed are a) a weakly cemented and b) well cemented sub-vertical sandstone dyke intrusion. The material infilling the intergranular pore-volumes are interpreted as spalls of mudstone host strata that have become entrained during the sandstone intrusion formation, and have become compacted around the quartz and feldspar grains.

Supplementary Material - Tables

Table S.1. Moreno Gulch & Marca Canyon - Structural Field Measurements of Sandstone Intrusions

GR (Latitude)	GR (Longitude)	Locality	Sub-Location	Structure no.	Type of structure	Av. Width (m)	Length (m)	Av. Strike	Av. Dip	Dyke Separation	Dyke Spacing (m)
36°42'28.68"N	120°43'0.80"W	MC1	n/a	1	Dyke	0.2	n/a	293	73		
36°42'30.08"N	36°42'30.08"N	MC2	n/a	2	Dyke	0.15	n/a	45	74	2 to 3	5.7
36°42'30.08"N	36°42'30.08"N	MC2	n/a	3	Dyke	0.15	n/a	61	195	3 to 4	22
36°42'30.08"N	36°42'30.08"N	MC2	n/a	4	Dyke	0.25	n/a	50	80		
36°43'55.17"N	120°43'57.00"W	MG1	Ridge 1	1	Dyke	0.75	43.3	59	79	1 to 2	7.6
36°43'54.92"N	120°43'57.03"W	MG1	Ridge 1	2	Dyke	1.8	50.7	246	88	2 to 3	2.3
36°43'54.81"N	120°43'56.95"W	MG1	Ridge 1	3	Dyke	1.1	60.2	71	78	3 to 4	21
36°43'54.21"N	120°43'56.37"W	MG1	Ridge 1	4	Dyke	0.8	65.6	78	88	4 to 5	14.3
36°43'53.64"N	120°43'56.45"W	MG1	Ridge 1	5	Dyke	2.4	99.6	67	73		
36°43'51.26"N	120°43'58.67"W	MG2	Ridge 2	1 to 4	Dyke	0.38	20	79	40	1-4 to 5-8	12
36°43'51.77"N	120°43'59.02"W	MG2	Ridge 2	5 to 8	Dyke	0.24	20	247	49	8 to 9	22
36°43'52.54"N	120°43'59.20"W	MG2	Ridge 2	9	Dyke	3.2	30.6	51	73	9 to 10	9.7
36°43'53.07"N	120°43'58.86"W	MG2	Ridge 2	10	Dyke	2.4	40.6	65	84	10 to 12	29
36°43'53.53"N	120°43'59.35"W	MG2	Ridge 2	11	Sill	0.25	29	170	44		
36°43'53.82"N	120°43'59.78"W	MG2	Ridge 2	12	Dyke	3.2	44.4	59	75		
36°43'50.50"N	120°44'3.73"W	MG3	Ridge 4	1	Dyke	7.0	46.3	67	52	1 to 2	32
36°43'51.52"N	120°44'4.17"W	MG3	Ridge 4	2	Dyke	3.6	50.1	253	73	2 to 3	11
36°43'51.95"N	120°44'4.37"W	MG3	Ridge 4	3	Dyke	1.0	41	69	82	3 to 4	7.5
36°43'52.21"N	120°44'4.50"W	MG3	Ridge 4	4	Dyke	3.0	46	239	83		

Av.is average, MC is Marca canyon, MG is Moreno Gulch.

Table S.2. Marca Canyon & Escarpados Canyon - Structural Field Measurements of Carbonate Mounds

GR (Latitude)	GR (Longitude)	Locality	Structure no.	Width (m)	Length (m)	Av. Strike	Av. Dip
36°38'34.24"N	120°41'40.85"W	EC1	EC1	A	1.2	7.7	121
36°38'34.37"N	120°41'41.17"W	EC1	EC1	B	7.2	2.9	93
36°38'34.57"N	120°41'41.59"W	EC1	EC1	C	5.7	2.5	99
36°38'34.87"N	120°41'41.99"W	EC1	EC1	D	2.7	7.6	n/a
36°38'34.75"N	120°41'42.24"W	EC1	EC1	E	4	1.6	85
36°38'34.91"N	120°41'42.35"W	EC1	EC1	F	3.1	1.1	138
36°38'35.13"N	120°41'42.63"W	EC1	EC1	G	1.1	2.8	121
36°38'34.99"N	120°41'42.80"W	EC1	EC1	H	1.1	2.2	n/a
36°42'30.30"N	120°43'0.42"W	MC3	A	2.5	2.7	n/a	n/a
36°42'30.30"N	120°43'0.42"W	MC3	B	5	3.7	n/a	n/a
36°42'30.30"N	120°43'0.42"W	MC3	C	4.5	6.5	n/a	n/a
36°42'30.30"N	120°43'0.42"W	MC3	D	3.1	3.8	n/a	n/a
36°42'30.30"N	120°43'0.42"W	MC3	E	6.3	7.3	n/a	n/a
36°42'30.30"N	120°43'0.42"W	MC3	F	3.0	3.5	n/a	n/a

AC is Average; MC is Marca canyon; EC is Escarpados Canyon.